

Precision Measurement of Electroproduction of π^0 near Threshold

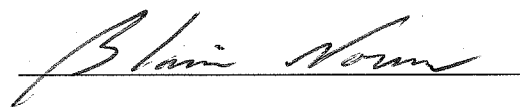
Khem Chirapatpimol
Chiang Mai, Thailand

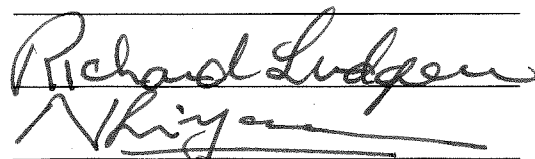
B.S., Chiang Mai University, 2004

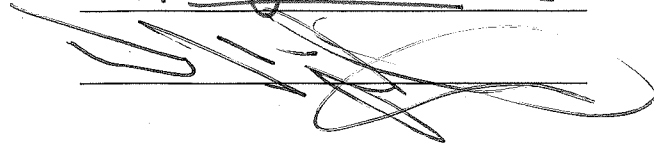
A Dissertation presented to the Graduate Faculty of the
University of Virginia in Candidacy for the Degree of
Doctor of Philosophy

Department of Physics

University of Virginia
May, 2012


Blair Norn


Richard Ludger


N. Hiyama

**Precision Measurement of Electroproduction of π^0
near Threshold ABSTRACT**

Electromagnetic production of neutral pions near threshold is the most basic, lowest energy reaction in which a new hadron is created. The electromagnetic interaction is well understood so measurements of this reaction can yield direct insight into the hadronic production mechanism.

During the past three decades there have been many developments in both the measurement and theory of threshold pion production, starting with measurements of photoproduction, $p(\gamma, \pi^0)p$, at Saclay in 1986 and at Mainz in 1990. These measurements indicated a surprising discrepancy with so-called Low Energy Theorems (LETs) which are based on quite fundamental symmetries and considerations. Chiral Perturbation Theory (ChPT) is an effective field theoretic description of the nuclear force which contains the underlying symmetries of the force but deals with nucleons and pions rather than quarks and gluons. It has the advantage of being applicable at low energies but requires tuning some parameters to experimental data. Once these parameters have been determined ChPT predicts how the reaction should behave as a function of the kinematic variables. When applied to the reaction, $p(\gamma, \pi^0)p$, near threshold it explained the discrepancy with the LETs and made predictions for electroproduction, $p(e, e')\pi^0$. Electroproduction measurements at Mainz in the 1990's showed a clear discrepancy with these predictions of ChPT; with parameters determined from one set of kinematics the data for a second set lay far from the predicted value. However, recently completed measurements at Mainz disagreed with their previous measurements.

In the experiment presented here, measurements of neutral pion electroproduction,

$p(e, e'p)\pi^0$, were made in fine bins of momentum transfer, Q^2 , between $Q^2 = 0.05 \text{ [GeV/c]}^2$ and $Q^2 = 0.15 \text{ [GeV/c]}^2$ and of center-of-mass energy, W , between $0 \leq W \leq 30 \text{ MeV}$ (above threshold). The experiment was performed in Hall A at the Jefferson Laboratory. Scattered electrons were detected in one of the two High Resolution Spectrometers while the recoiling protons were detected in the BigBite spectrometer.

The results of the present experiment agree within uncertainties with the recent Mainz measurements and extend in W significantly beyond those measurements. The present data show significant disagreement with some terms in the cross section above $Q^2 \approx 0.10 \text{ [GeV/c]}^2$: the total cross section, (A_0^{T+L}) , and the transverse-transverse cross section, (A_0^{TT}) . For $W \geq 5 \text{ MeV}$ the disagreement is very strong and consistent. Whether fitting new ChPT parameters to the recent data or adding more terms to the calculations would improve the agreement remains to be seen.

Acknowledgements

In writing this dissertation I received big big help on editing, proof reading, comment and translating English to English from Cole Smith, Richard Lindgren and my advisor, Blaine Norum. I also want to thank my committee members Douglas Higinbotham and Nilanga Liyanage for taking the time to read and comment on my dissertation, and be on my committee.

I would also like to thank the other people who were involved in the experiment. But, let me start by apologizing if I forget to mention anyone: Brad Sawatzky, Bryan Moffit, Kalyan Allada, Mitra Shabestari, Ole Hansen, Xin Qian , Vince Sulkosky, Vladimir Nelyubin, Jack Segal, Ed Folts and his crew, JLAB staff, and the accelerator crew.

Finally, I would like to thank my parents for their love and support.

Contents

1	Introduction	1
2	ChPT Introduction	9
2.1	QCD	9
2.2	Effective Field Theory	12
2.3	ChPT	13
2.4	Phenomenological Models	16
3	Experimental Apparatus	18
3.1	Target	20
3.2	Left HRS	23
3.3	BigBite Spectrometer	26
3.4	Trigger	29
4	Data Analysis	35
4.1	Calibration	35
4.1.1	Beam Energy	35
4.1.2	Electron Detection using Left HRS (LHRS)	37
4.1.3	Proton Detection using BigBite	41
4.1.3.1	BigBite ADC	41
4.1.3.2	BigBite TDC	42
4.1.3.3	BigBite Wire Chamber	43
4.1.3.4	BigBite Optics	44
4.1.4	Time of Flight	50
4.2	Efficiency	54
4.2.1	BigBite MWDC Track Finding Efficiency	54
4.2.2	BigBite MWDC Plane Hit Efficiency	55
4.2.3	LHRS VDC,TDC and tracking	55
4.2.4	Dead Time and EDTM	55
4.3	Simulation	59
5	Cross Section and Radiative Correction	70
5.1	Background Subtraction	72
5.2	Radiative Corrections	76
5.3	Cross Section Measurement	77
6	Results and Conclusion	80

6.1 Conclusion	84
Bibliography	86

List of Figures

1.1	Mainz photoproduction differential cross section	3
1.2	Mainz π^0 photoproduction total cross section	4
1.3	Real part of the electric dipole amplitude E_0^+ for π^0 photoproduction	5
1.4	Mainz π^0 electroproduction total cross section data	6
1.5	Mainz π^0 electroproduction S-wave and P-wave amplitudes	7
3.1	Layout of CEBAF	19
3.2	Layout of Hall A	19
3.3	Liquid target ladder	20
3.4	Solid target ladder	21
3.5	Target ladder	21
3.6	Target chamber	22
3.7	A helium balloon	23
3.8	Layout of HRS	25
3.9	Layout of VDC	26
3.10	Layout of Bigbite	28
3.11	Bigbite magnet and structure holding MWDCs and scintillators	29
3.12	Trigger diagram for left HRS	30
3.13	Trigger diagram for BigBite E-plane	31
3.14	Trigger diagram for BigBite dE-plane	32
3.15	Diagram of coincidence trigger	33
4.1	Beam energy determination	36
4.2	Beam energy vs run number	37
4.3	VDC time spectra	39
4.4	HRS sieve	40
4.5	W of Ta target	41
4.6	BigBite E ADC vs dE ADC	42
4.7	MWDC first plane residue	44
4.8	midplane	45
4.9	dvz 1	47
4.10	dvz 2	48
4.11	missing mass	50
4.12	Time of flight	52
4.13	missing mass in time window -5 to 5 ns	53
4.14	missing mass in time window -5 to 5 ns	53

4.15	missing mass	54
4.16	T5 Dead Time	56
4.17	Difference between T5 dead time and T6 dead time	57
4.18	EDTM dead time	57
4.19	Difference between T5 dead time and EDTM dead time	58
4.20	Histogram of difference between T5 dead time and EDTM dead time	58
4.21	data-simulation magnet and wmdc comparison	60
4.22	Target Coordinate System	62
4.23	Acceptance of the LHRS and the BigBite	63
4.24	LHRS ϕ_{tg} versus dp/p_0	64
4.25	LHRS θ_{tg} cut on ϕ_{tg} and dp/p_0 grid	65
4.26	BigBite ϕ_{tg} versus θ_{tg}	66
4.27	BigBite momentum cut on ϕ_{tg} and θ_{tg} grid	67
4.28	LHRS dp/p_0 versus Q^2	68
4.29	W cut on LHRS dp/p_0 and Q^2 grid	69
5.1	A schematic of the electron scattering and pion-nucleon reaction plane. . . .	71
5.2	missing mass $W_{th} < W < W_{th} + 2 \text{ MeV}$ middle 4cm of 6cm target	73
5.3	missing mass vs W of liquid hydrogen target	74
5.4	missing mass vs W of dummy target	74
5.5	Count of missing mass in region $\pm 10 \text{ MeV}$ around π^0 mass	76
5.6	EXCLURAD radiative correction	77
6.1	Measured total differential cross section versus DMT simulation	80
6.2	Legende fit	81
6.3	Total cross section	83

List of Tables

2.1	Quark flavors and their charge and masses	10
3.1	The design characteristic of the HRS.	24
3.2	Trigger	30
3.3	Kinematic setup summary	33
4.1	Efficiency of run number 4760	59
5.1	Q^2 and ϕ_e bins	78

Chapter 1

Introduction

Quantum Chromodynamics (QCD), the fundamental theory of strong interactions, has been very successful in describing high energy scattering processes where the interaction of quarks and gluons can be treated perturbatively. But for low energy scattering processes, where quarks and gluons are confined, traditional perturbation theory is useless because the strong coupling has increased to where higher order terms cannot be ignored. One alternative at low energy is Chiral Perturbation Theory (ChPT) which has been quite popular and successful. ChPT is an effective field theory (EFT) that is applicable at low energies. The basic idea of ChPT is to expand the Lagrangian in terms of pion and baryon fields instead of quark and gluon fields, while retaining the symmetries of QCD. Specifically, the Lagrangian is expanded in terms of ratios of low pion momenta and hadron masses. The coefficients of each term, called low energy constants (LEC), are obtained from experimental data. Once the LECs are determined the theory possesses predictive power.

Analysis of measurements from Mainz [1] and Saskatoon [2] of the photoproduction reaction $p(\gamma, \pi^0)p$ at the pion production threshold have determined that the s -wave multipole (E_{0+}) is well reproduced by ChPT (after adding loop terms [3]). On the other hand, cross section measurements of electroproduction at Mainz [4] and the Netherland National

Institute for Nuclear and High Energy Physics (NIKHEF) [5] where ChPT LEC's were fitted at four momentum transfers $Q^2 = 0.1 \text{ [GeV/c]}^2$, disagreed significantly with ChPT predictions at $Q^2 = 0.05 \text{ [GeV/c]}^2$ [6, 7]. The important question is whether the theory is fundamentally wrong or the data are incorrect or both. This discrepancy is potentially very significant. The purpose of our experiment is to remeasure the cross section with fine bins in W (center of mass energy of the pion-nucleon system) and Q^2 and to extend the range to higher W and Q^2 for comparison with theory. By extending the measurements over a broad range we can compare with the earlier measurements and use the systematics of our data to determine new low energy constants (LECs) and determine the limits of the Chiral Dynamics calculation.

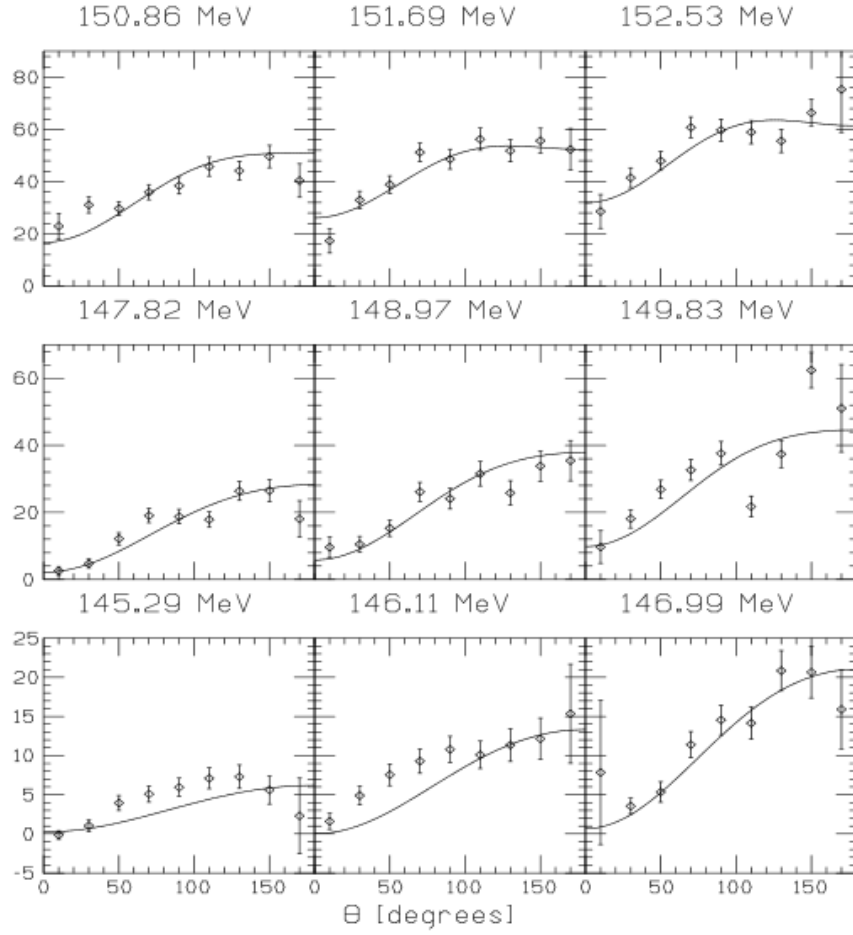


Figure 1.1: Mainz π^0 photoproduction differential cross sections in the threshold region (in nb/sr) for the lowest 9 values of the photon lab energy E , versus the cm scattering angle θ . The solid line is the prediction of ChPT; the data are from ref. [8]. This figure is taken from ref. [3].

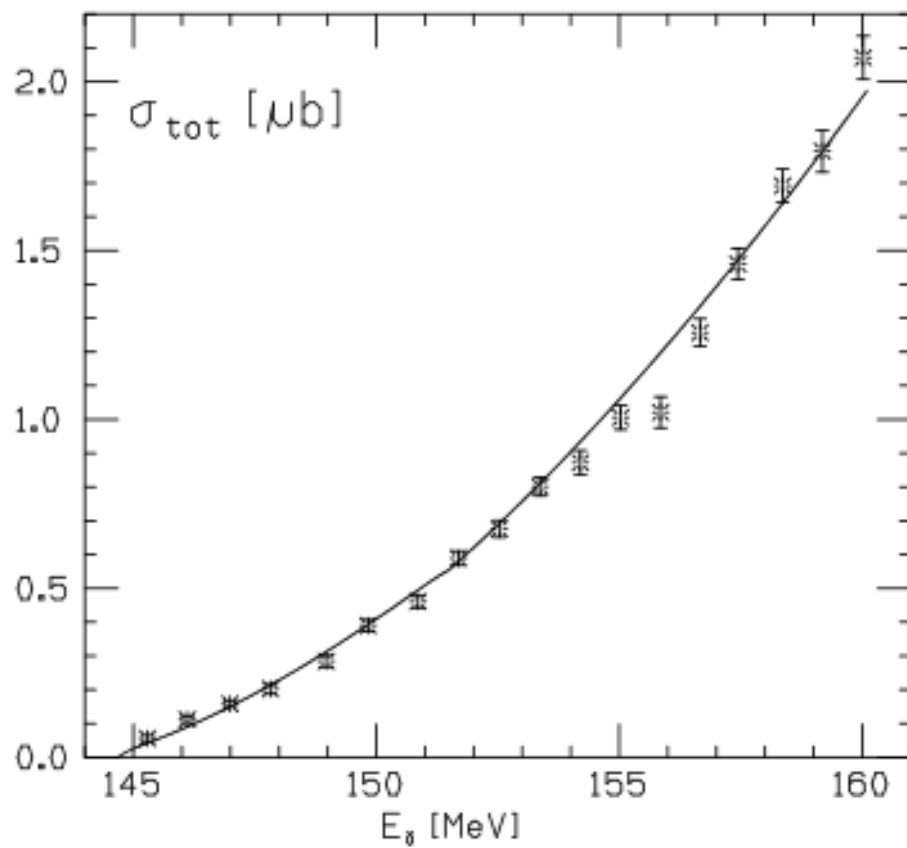


Figure 1.2: Mainz π^0 photoproduction total cross section in the threshold region (in pb) versus E_γ . The solid line the prediction is ChPT; the data are from ref. [8]. This figure is taken from ref. [3].

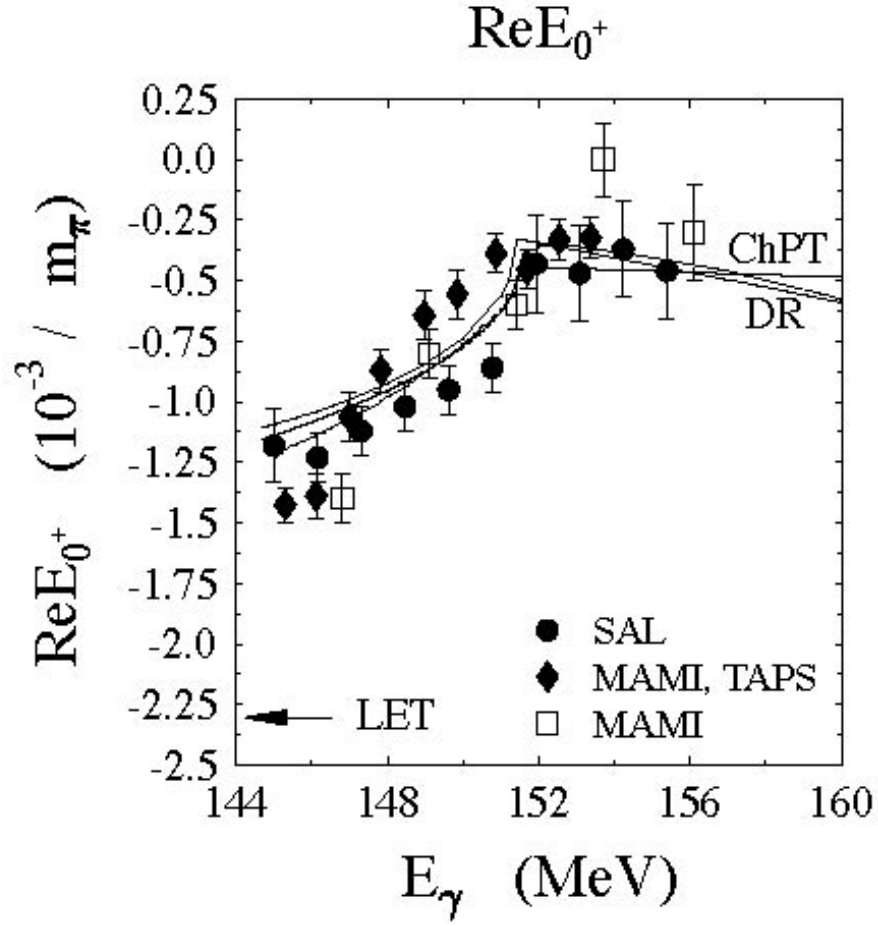


Figure 1.3: Real part of the electric dipole E_0^+ of π^0 photoproduction. The arrow shows an old low energy theorem calculation[9, 10] $-2.3 \times 10^{-3}/m_\pi$. ChPT successfully fitted the data after the addition of a loop correction term. This figure is taken from ref. [11].

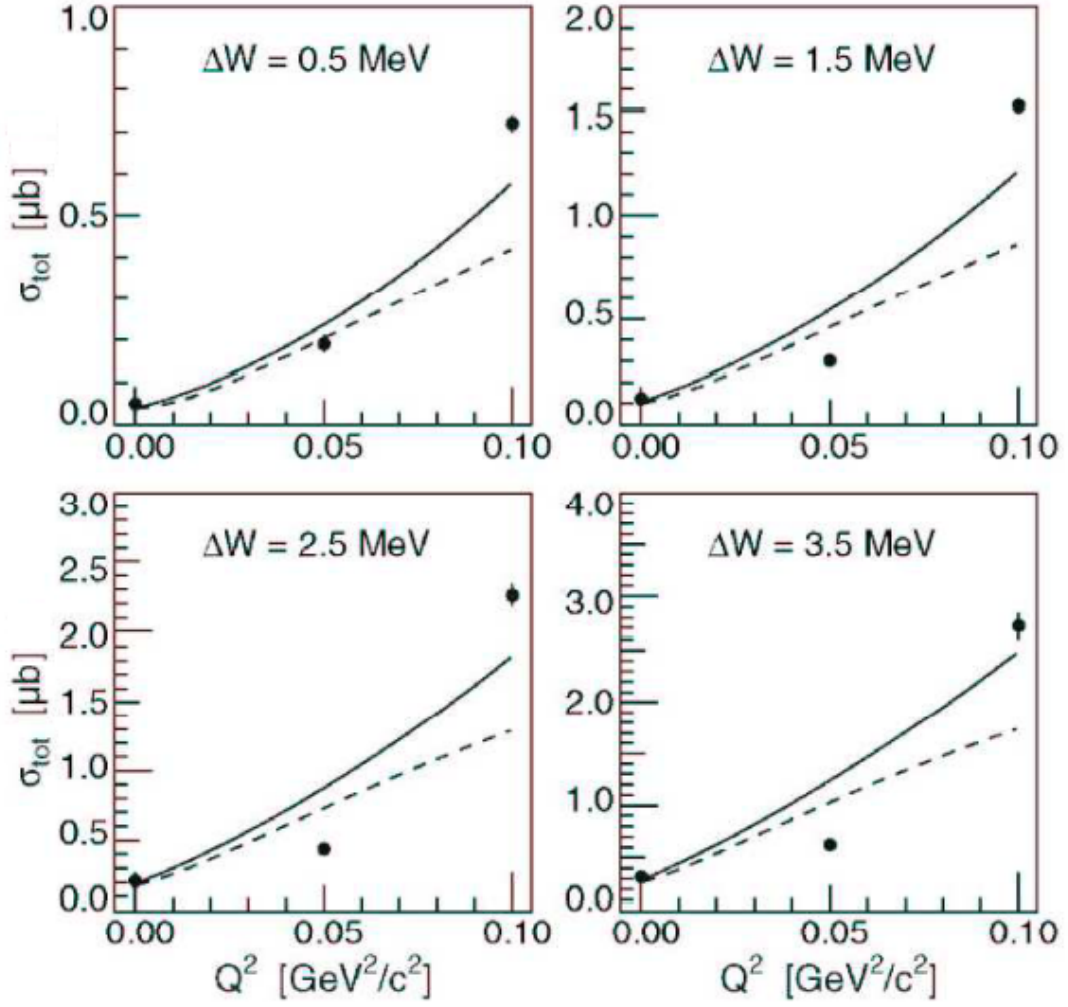


Figure 1.4: Mainz π^0 electroproduction data: The W and Q^2 dependence of the total cross section at $\epsilon = 0.8$. The solid(dashed) line is the prediction of ChPT(MAID). This figure is taken from ref. [7].

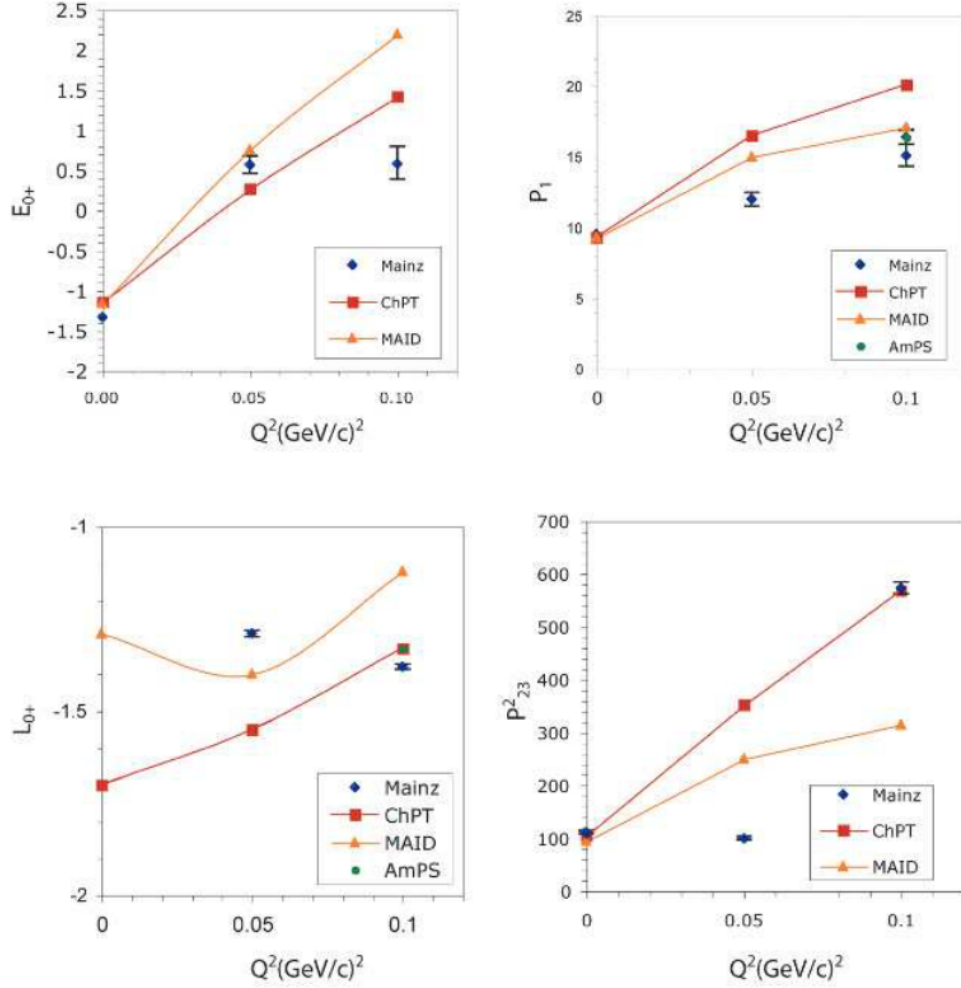


Figure 1.5: Mainz π^0 electroproduction data: On the left the S-wave amplitudes E_{0+} and L_{0+} are plotted versus Q^2 . On the right the P-wave amplitude P_1 and the combination $P_{23}^1 = 1/2(P_2^2 + P_3^2)$ are plotted versus Q^2 . The Mainz data are from ref. [4] and [7]. The NIKHEF data are from ref. [12]. This figure is taken from ref. [13].

The experiment presented here, the measurement of cross section and asymmetry of the reaction $p(\vec{e}, e'p)\pi^0$ near threshold at four momentum transfers (Q^2) in the range of $0.045 \leq Q^2 \leq 0.15$ $[\text{GeV}/c]^2$ and center of mass energy of the $\pi - N$ system (W) from

threshold to 20 MeV above threshold, was performed in Hall A of the Thomas Jefferson National Accelerator Facility (JLAB) in 2008. The results provide a testing ground for ChPT.

Chapter 2

ChPT Introduction

This chapter starts with a short introduction to QCD, Effective Field Theories and ChPT. It finishes with a discussion of the unitary MAID and DMT models which were also used in the analysis, especially in simulations used to model the detector acceptance.

2.1 QCD

QCD is a non-abelian gauge theory of the strong interaction with color $SU(3)$ as the underlying gauge group. The matter fields of QCD are quarks, which are spin 1/2 fermions that carry color charge and have six different flavors: up, down, strange, charm, top and bottom. A hallmark of QCD is asymptotic freedom [14, 15] where the interaction strength between quarks becomes weaker as energy increases and distances decrease. This implies that only in the short distance limit can perturbative methods be legitimately employed. For a guide to the literature on QCD, see ref. [16].

Table 2.1: Quark flavors and their charge and masses from ref. [17]

Flavor	Mass[MeV/c ²]	Charge
u	1.7 to 3.1	2e/3
d	4.1 to 5.7	-e/3
s	80 to 130	-e/3
c	1180 to 1340	2e/3
t	172,900 ± 600 ± 900	2e/3
b	4130 to 4370	-e/3

In the case of the top quark, the first uncertainty is statistical in origin and the second is systematic.

The gauge bosons, which also carry color, are the gluons, each with field $A_{a\mu}$. Classical chromodynamics is defined by the Lagrangian

$$\mathcal{L}_{QCD} = \bar{q}(i\gamma^\mu D_\mu - m)q - \frac{1}{4}G_{a\mu\nu}G_a^{\mu\nu} \quad (2.1)$$

where q is quark field, γ^μ are Dirac matrices. The repeated indices are summed over. The gauge field strength tensor is

$$G_{a\mu\nu} = \partial_\mu A_{a\nu} - \partial_\nu A_{a\mu} - g_3 f_{abc} A_{b\mu} A_{c\nu} \quad (2.2)$$

where g_3 is the $SU(3)$ gauge coupling parameter, and the quark covariant derivative is

$$D_\mu q \equiv (\partial_\mu + ig_3 A_\mu)q \quad (2.3)$$

The Lagrangian in eq. (2.1) is invariant under local transformation

$$q(x) \rightarrow \exp(-i\omega_a(x)\frac{\lambda_a}{2})q(x) = U(x)q(x) \quad (2.4)$$

$$q^\dagger(x) \rightarrow q^\dagger(x)U^\dagger(x) \quad (2.5)$$

$$A_\mu \equiv A_{a\mu} \frac{\lambda_a}{2} \rightarrow A'_\mu = UA_\mu U^\dagger + \frac{i}{g_3} \partial_\mu UU^\dagger \quad (2.6)$$

where ω_a are smooth real function in Minkowski space, and λ_a denote Gell-Mann matrices acting in color space.

The field q can be projected to its chiral components q_R and q_L

$$q = q_R + q_L, \quad q_R = P_R q, \quad q_L = P_L q \quad (2.7)$$

where

$$P_R = \frac{1}{2}(\mathbf{I} + \gamma_5) = P_R^\dagger, \quad P_L = \frac{1}{2}(\mathbf{I} - \gamma_5) = P_L^\dagger \quad (2.8)$$

$$\gamma_5 = \gamma^5 = i\gamma^0\gamma^1\gamma^2\gamma^3 = \gamma_5^\dagger \quad (2.9)$$

The Lagrangian then becomes

$$\mathcal{L}_{QCD} = \bar{q}_L i\gamma^\mu D_\mu q_L + \bar{q}_R i\gamma^\mu D_\mu q_R - \bar{q}_L m q_R - \bar{q}_R m q_L - \frac{1}{4} G_{a\mu\nu} G_a^{\mu\nu} \quad (2.10)$$

In the chiral limit, $m \rightarrow 0$, for 3 light quarks, the Lagrangian would be invariant under independent global left- and right-handed rotations

$$q_L \rightarrow \exp(-i\omega_{La} \frac{\lambda_a}{2}) q_L \quad (2.11)$$

$$q_R \rightarrow \exp(-i\omega_{Ra} \frac{\lambda_a}{2}) q_R \quad (2.12)$$

According to Goldstone's theorem [18], the breakdown of the chiral symmetry $SU(3)_L \times SU(3)_R$

implies eight massless pseudoscalar Goldstone bosons. In nature, the eight lightest strongly interacting particles are the pions (π^+, π^0, π^-) and kaons (K^+, K^-, K^0, \bar{K}^0) and the eta (η). Their finite but small masses are related to the explicit chiral symmetry breaking by quark masses. Given the vanishing of the Goldstone boson masses in the chiral limit and their vanishing interactions in the zero-energy limit, a derivative and quark mass expansion is the natural scenario for an EFT. This effective field theory method is called chiral perturbation theory.

2.2 Effective Field Theory

EFT has a wide range of application; see ref. [19] for some examples. Here the introduction to EFT is from ref. [20]. The EFT is a low-energy approximation to the underlying fundamental theory and valid under some energy scale Λ . An EFT uses the degrees of freedom suitable for the low-energy domain of interest, for example, by neglecting particles which are too heavy to be produced at low energy. The degrees of freedom can be entirely different from the underlying theory. For example, low energy hadronic physics calculations use mesons (π, K, η) and baryons ($p, n, \Sigma, \Xi, \Lambda$) instead of quarks and gluons. However the Lagrangian has to take the most general form consistent with the symmetries of the underlying theory. The number of terms, each with its own coefficients, called low energy constants (LEC), used in expanding the Lagrangian (like any approximation) determines the accuracy in a certain energy domain. The EFT is used to calculate physical observables in terms of an expansion in p/Λ , where p is generally energy, momentum or a mass that is smaller than the scale Λ . The number of terms in the expansion contributes to an accuracy which corresponds to the number of terms in the Lagrangian. For a renormalization scheme,

all counter terms which abide the same symmetries are added. LECs should in principle be calculated from the underlying theory or in practice, where the theory cannot be solved (like QCD), be fitted to data. Once the LECs are determined, the EFT possesses predictive power.

One of the best known examples of EFT is Fermi's theory of beta decay. In the Standard Model, neutron beta decay $n \rightarrow pe^-\bar{\nu}_e$ is described via an intermediate massive W boson, $M_W \simeq 80 \text{ GeV}/c^2$, the W boson propagator in low energy limit $\frac{1}{q^2 - M_W^2} \rightarrow -\frac{1}{M_W^2}$. In Fermi's theory, the degrees of freedom are reduced from the underlying weak interaction, since the W boson is excluded and the energy scale Λ is now M_W , the mass of the W boson.

2.3 ChPT

In ChPT, the effective Lagrangian consists of the asymptotically observed fields, the pions and the nucleons, and has all the properties of QCD, i.e. underlying symmetries of QCD, the spontaneous breakdown of the chiral symmetry and the Ward-Takahashi identities. In the tree calculation (Feynman diagram), it is mandatory to go one order further (one-loop) beyond leading order, due to the fact that in the chiral limit of vanishing quark masses the pseudoscalar Goldstone bosons become massless and lead to infrared singularities in certain Green functions. Also, the loop terms give rise to non-zero beam polarization asymmetries which have been clearly measured to be non-zero [21].

ChPT was studied systematically first by Gasser and Leutwyler [22] for purely mesonic systems. It was later extended to include baryons (nucleons) by Gasser, Sainio and Svarc [23] (referred to as Baryon ChPT, BChPT). This effective lagrangian has a power series expansion in derivatives and the chiral symmetry breaking quark mass matrix. Higher

dimensional operators are suppressed by inverse powers of the chiral symmetry breaking scale $\Lambda_x \simeq 4\pi F_\pi \sim 1 \text{ GeV}$ (with $F_\pi = 93 \text{ MeV}$, the pion decay constant). Thus, a term with two additional derivatives will be suppressed by M_B^2/Λ_x^2 , where M is the π , K or η mass. The baryon mass is roughly of the same size as chiral-symmetry-breaking scale $M_B/\Lambda_x \sim O(1)$, so the higher order terms are not suppressed. To solve this problem, Manohar and Jenkins used the formalism developed by Georgi for the study of heavy quarks [24], the theory is referred to as Heavy BChPT (HBChPT) [25]. In this approach [26], the baryon momentum is separated into a large piece mv_μ and a small off-shell momentum l_μ

$$p_\mu = mv_\mu + l_\mu \quad (2.13)$$

where $v^2 = 1$. With the projection operator $P_v = \frac{1}{2}(1 + \not{v})$, Ψ the nucleon field is decomposed into

$$\Psi(x) = e^{-imv \cdot x} (H(x) + h(x)) \quad (2.14)$$

with

$$\not{v}H = H, \quad \not{v}h = -h \quad (2.15)$$

Consider the πN Lagrangian, built of nucleon field Ψ and pion field U which is parametrized in the σ -model gauge by.

$$U = u^2 = (\sigma + i\phi)/F, \quad \sigma^2 + \phi^2 = F^2, \quad (2.16)$$

with F being the pion decay constant in the chiral limit. The pion and nucleon field

transform under the chiral operator $SU((2)_L \times SU(2)_R)$ as

$$U \rightarrow g_R U g_L^\dagger \quad (2.17)$$

$$\Psi \rightarrow K(U, g_L, g_R) \Psi \quad (2.18)$$

$$K(U, g_L, g_R) = \sqrt{g_L U^\dagger g_R^\dagger g_R} \sqrt{U} \quad (2.19)$$

where $g_{L,R} \in SU(2)_{L,R}$. To lowest order in derivatives and quark masses, the effective πN Lagrangian reads

$$\mathcal{L} = \mathcal{L}_{\pi N}^{(1)} + \mathcal{L}_{\pi\pi}^{(2)} \quad (2.20)$$

where $\mathcal{L}_{\pi\pi}^{(2)}$ is the gauged non-linear σ -model for the pion (general meson Lagrangian is given by [27] $\mathcal{L}_{\pi\pi}^{(2)} = \frac{F^2}{4} \text{Tr}[D_\mu U (D^\mu U)^\dagger + \chi^\dagger U + \chi U^\dagger]$) and $\mathcal{L}_{\pi N}^{(1)}$ is the most general Lagrangian with the smallest number of derivatives is given by [23]

$$\mathcal{L}_{\pi N}^{(1)} = \bar{\Psi}(i\not{D} - \not{m} + \frac{\not{g}_A}{2}\not{\mathcal{A}}\gamma_5)\Psi \quad (2.21)$$

where $D_\mu = \partial_\mu + \Gamma_\mu$ is the covariant derivative with Γ_μ the chiral connection and $u_\mu = iu^\dagger \nabla_\mu u^\dagger$ and \not{m} and \not{g}_A denote m and g_A in chiral limit. With (2.14) and the equation of motion

$$h = \frac{1}{2}(1 - \not{v})\frac{1}{2\not{m}}(i\not{D} + \frac{\not{g}_A}{2}\not{\mathcal{A}}\gamma_5)H + O(1/\not{m}^2) \quad (2.22)$$

and eliminating this small-component field h by substituting for H in (2.21), the Lagrangian becomes

$$\mathcal{L}_{\pi N}^{(1)} = \bar{H}(i\not{v} \cdot D + \not{g}_A S \cdot u)H + \frac{1}{2\not{m}}\bar{H}(i\not{D} + \frac{\not{g}_A}{2}\not{\mathcal{A}}\gamma_5)\frac{1 - \not{v}}{2}(i\not{D} + \frac{\not{g}_A}{2}\not{\mathcal{A}}\gamma_5)H + O(1/\not{m}^2) \quad (2.23)$$

where the spin operator $S_\mu = \frac{1}{2}i\gamma_5\sigma_{\mu\nu}v^\nu$. All momenta are now small on the scale of chiral symmetry breaking scale $\Lambda_\chi \sim 1 \text{ GeV}$ and loop diagrams are now suppressed by power of q^2 . The Feynman rules can be derived from the Lagrangian (2.23). To leading order the pion-nucleon and photon-nucleon vertices are independent of \hat{m} and this leads to a consistent power counting scheme as discussed in detail in ref. [25], but they have corrections suppressed by powers of \hat{m} and momentum.

For our interest, in the reaction $\gamma^* + p \rightarrow \pi^0 + p$ where γ^* is the virtual photon, the expansion of the S-wave multipoles E_{0+} and L_{0+} is given to three orders in small momenta and the five combinations of P-wave multipoles to two orders in ref. [28, 29] where LECs were fitted to the $Q^2 = 0.1 \text{ [GeV/c]}^2$ data from Mainz[4] and NIKHEF[5].

2.4 Phenomenological Models

The phenomenological models, MAID 2007 [30] (referred to as MAID) and DMT [31] are used for comparison with ChPT.

The MAID unitary isobar model was developed to analyze the world data on pion photoproduction and electroproduction. The model contains both a background and resonance terms. The background is unitarized according to the K-matrix prescription. The resonances are described in unitarized Breit-Wigner forms.¹

The Dubna-Mainz-Taipei (DMT) model starts from an effective chiral Lagrangian like ChPT. However, they differ from ChPT in their approach to calculating the scattering amplitudes. In DMT, the effective Lagrangian is used to construct a πN potential for use

¹The Breit-Wigner distribution, which is most often used to model resonances, is a probability distribution in the form $[(E^2 - M^2)^2 + M^2\Gamma^2]^{-1}$, where E is the CM energy that produces the resonance, M is the mass of the resonance, and Γ is the resonance width.

in the scattering equation. The solutions of the scattering equation will include rescattering effects to all orders and thereby unitarity is ensured, while crossing symmetry is violated. Contributions of resonances are treated phenomenologically by using standard Breit-Wigner forms.

Chapter 3

Experimental Apparatus

The experiment (E04-007) was performed in JLab Hall A. The goals of this experiment were to measure the cross section and beam polarization asymmetry $A_{LT'}$ for the $p(\vec{e}, e'p)\pi^0$ reaction in the threshold region. Two beam energies, 1.192 and 2.322 GeV, were used during the experiment. The polarized electron beam is produced at the injector by illuminating a photocathode and then accelerating the ejected electrons to 45 MeV. The beam is then further accelerated in each of two superconducting linacs, through which it can be recirculated up to four times. The polarization was measured with a Møller polarimeter [32]. The beam energy, measured by bending the electrons in a magnetic field in the arc section of the beam line, was verified by measurement of scattered electrons from various targets including liquid hydrogen, liquid deuterium, carbon and tantalum. The left High Resolution Spectrometer (LHRS [32]) was used to detect scattered electrons, and the BigBite [33] to detect the recoil protons. The recoiling protons had low momenta (<500 MeV) so a new scattering chamber and helium bag were used to minimize energy loss. For more information about the beam line see ref. [32].

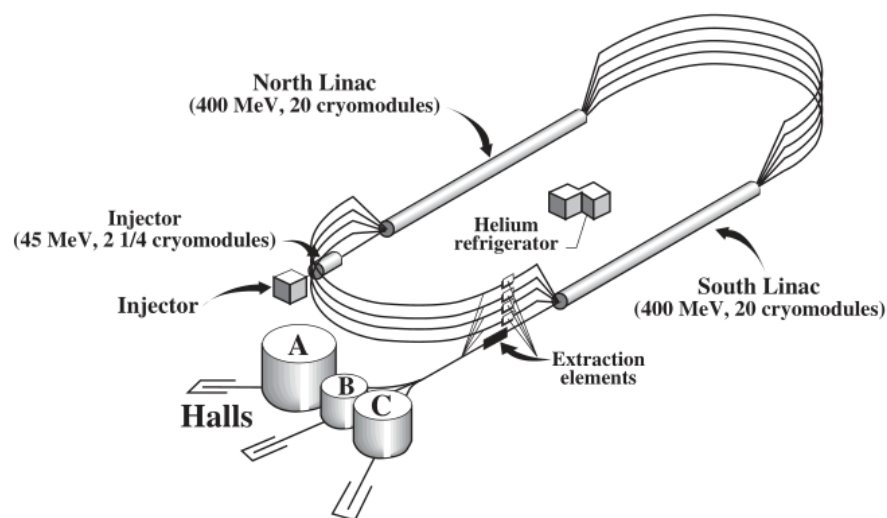


Figure 3.1: Layout of Continuous Electron Beam Accelerator Facility (CEBAF) at JLab.

Figure is from ref. [32].

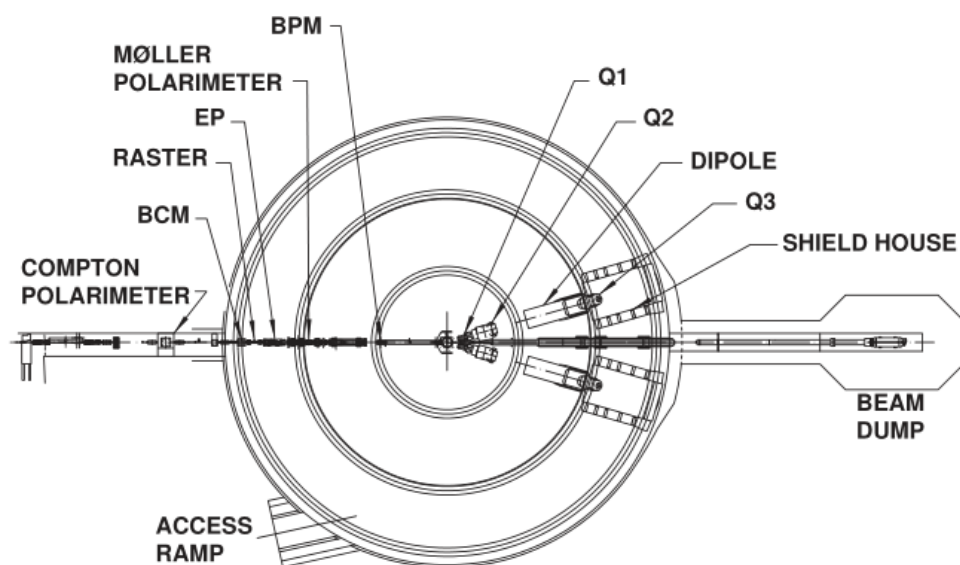


Figure 3.2: Layout of Hall A. During E04-007 the BigBite spectrometer replaced the right

HRS. Figure is from ref. [32].

3.1 Target

A 6 cm. liquid hydrogen target was used. The cell is made from aluminum A17075-T6 with thickness of entrance window 0.119 ± 0.003 mm, exit window 0.142 ± 0.006 mm and cell wall 0.142 ± 0.010 mm. Solid target foils, carbon, beryllium oxide and tantalum, were also used for vertex and energy calibrations. The new target scattering chamber with a thin titanium window for the BigBite side was used. The helium balloon was wedge shaped to fill the solid angle of the emerging protons from the target, and minimize air gaps at the front of the first multi-wire drift chamber. As shown in figure 3.7, the balloon provided a pure helium path for protons to minimize the energy loss and multiple scattering.



Figure 3.3: Liquid target ladder in target chamber with target cells (from top to bottom): liquid H_2 with collimator, liquid H_2 (main cell for π^0 production), liquid D_2 with collimator, liquid D_2 , spare and spare. Two aluminum foils at bottom are for dummy target runs. Figure is from ref. [34].



Figure 3.4: Solid target ladder which was mounted under the liquid target ladder in figure 3.3. From top to bottom, BeO, Tantalum, Carbon, Carbon with hole. Figure is from ref. [34].

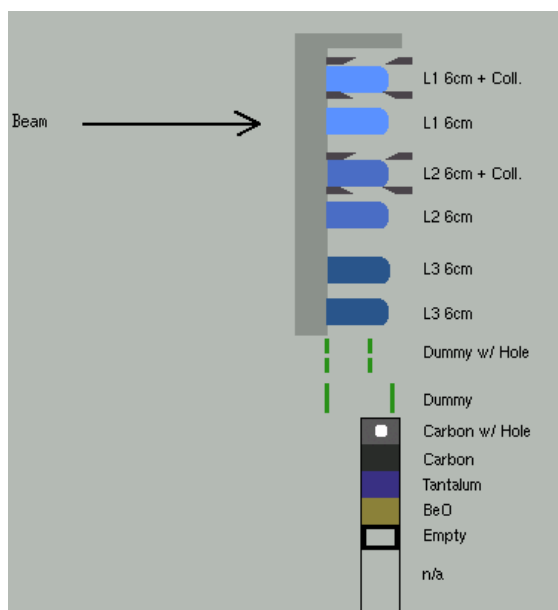


Figure 3.5: Target ladder in Hall A target control GUI.



Figure 3.6: Target chamber with flange insert and Ti window. The yellow coils of the BigBite magnet are seen at left. A He balloon was used to fill this air gap between the BigBite and the target chamber.



Figure 3.7: A helium balloon filled the gap between the BigBite magnet pole faces. The right side of balloon was connected to the target chamber when in taking data position.

3.2 Left HRS

The HRSs were designed for detecting charged particles with high resolution.

Table 3.1: The design characteristic of the HRS. The resolution values are for the full width half maximum. Table is taken from [32]

Configuration	QQDQ vertical bend
Bending angle	45°
Optical length	23.4 m
Momentum range	$0.3 - 4.0\text{ GeV}/c$
Momentum acceptance	$4.5\% < \delta p/p < +4.5\%$
Momentum resolution	$1 \times 10^4\text{ (GeV)}$
Dispersion at the focus (D)	12.4 m
Radial linear magnification (M)	-2.5
D/M	5.0
Angular range of left HRS	$12.5^\circ - 150^\circ$
Angular range of right HRS	$12.5^\circ - 130^\circ$
Angular acceptance (Horizontal)	$\pm 30\text{ mrad}$
Angular acceptance (Vertical)	$\pm 60\text{ mrad}$
Angular resolution (Horizontal)	0.5 mrad
Angular resolution (Vertical)	1.0 mrad
Solid angle at $\delta p/p = 0, y_0 = 0$	6 msr
Transverse length acceptance	$\pm 5\text{ cm}$
Transverse position resolution	1 mm

The magnets in the system include a pair of superconducting $\cos(2\theta)$ quadrupoles, a dipole, a third superconducting $\cos(2\theta)$ quadrupole. After the magnets, the detectors in the system are two Vertical Drift Chambers (VDCs), an S1 scintillator plane, a gas Cerenkov, and an S2 scintillator plane. The quadrupole magnets are used to focus the charged particle. The dipole magnet is used to bend the particle vertically and separate tracks according to momentum. The VDCs are used for reconstruction of the hit positions and local angles at the focal plane. Each VDC consists of one U and one V wire plane lie in the laboratory horizontal plane. The U wire and V wire orientations are 45° and -45° respect to the long edge of the plane. The VDCs were filled with an argon (62%) and ethane (38%) mixture. A charged particle ionizes the gas when passing through the VDCs. The ions then drift to the closest wire, and the drift time of the hit is recorded in a time-to-digital converter (TDC) which is then used for track reconstruction. Trigger scintillators in the S1 and S2 planes

consist of 6 overlapping paddles made of thin plastic scintillator. The S2 scintillators are used as the main trigger for the Left HRS which then are used to form a coincident trigger with the BigBite. Refer to ref. [32] for more details on Left HRS.

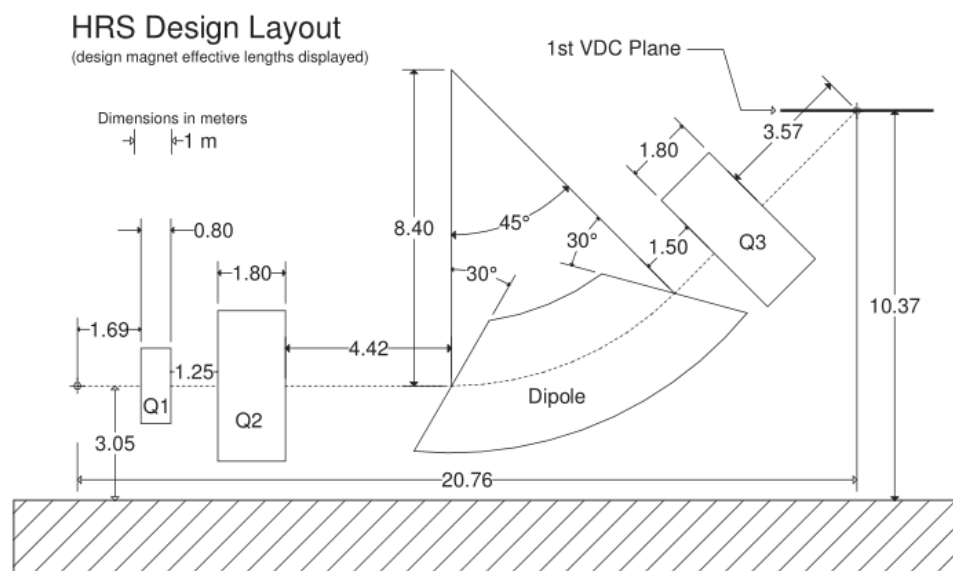


Figure 3.8: Layout of HRS shows dipole and quadrupoles and the first VDC. Figure is from ref. [32].

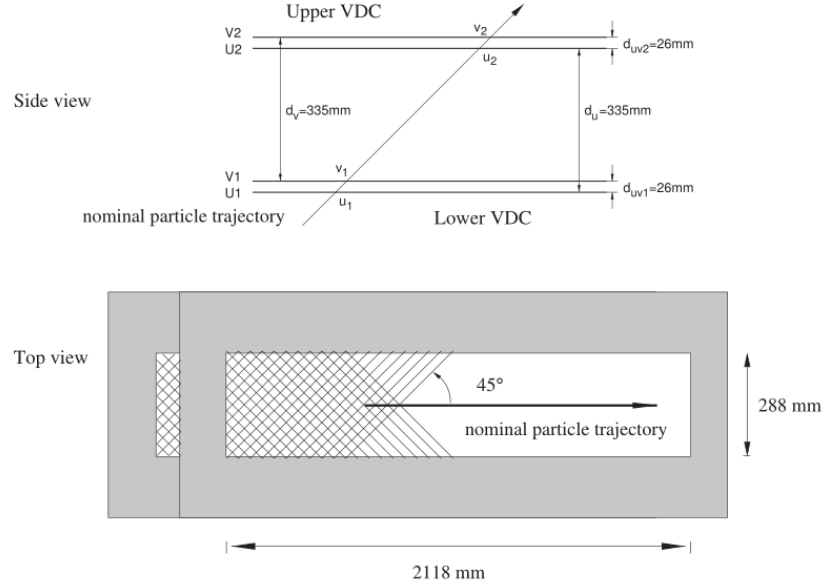


Figure 3.9: Schematic layout of a pair of Vertical Drift Chambers for one HRS (not to scale). The active area of each wire plane is rectangular and has a size of 2118 mm x 288 mm. The vertical distance between like wire planes is 335 mm. Figure is from ref. [32].

3.3 BigBite Spectrometer

BigBite consists of a single dipole magnet and a detector package behind the magnet. For this experiment, the detector package consisted of 2 multi-wire drift chambers (MWDC) for tracking, and 2 scintillator planes each consisting of 24 paddles for use in the coincidence trigger as shown in figure 3.10.

Each scintillator paddle is viewed by two photomultiplier tubes (PMT). Initial PMT gains were equalized by using minimum-ionizing peaks obtained from cosmic ray triggers. The high voltages applied to the PMTs were adjusted so that the analog-to-digital converter (ADC) signal spectra peaked at the same position for all PMTs. The 2 scintillator planes, dE

(3 mm thick) and E (30 mm thick) are complementary to each other, responding differently to different proton momenta. The E and dE thresholds were set to trigger on protons in a momentum range about 0.2 GeV to 0.5 GeV.

Each MWDC consists of three pairs of wire planes (six wire planes), having wire angles of 30° , -30° and 0° relative to horizontal. In each pair, the wires in the first plane are shifted 5 mm relative to the second plane. The distance between the wires in each plane is 1 cm. The MWDCs operate with a mixture of 50% Argon and 50% ethane. Extensive detail about the construction and specification of the MWDCs can be found in ref. [21, 35].

BigBite has a large angular and momentum acceptance that can fully cover the momentum range of the recoiling proton, corresponding to a threshold energy ΔW less than 10 MeV, in 3 settings: 43.5, 48.0 and 54.0 degree for most the Q^2 range measured. Refer to ref. [21],[35],[33] for more details on the BigBite.

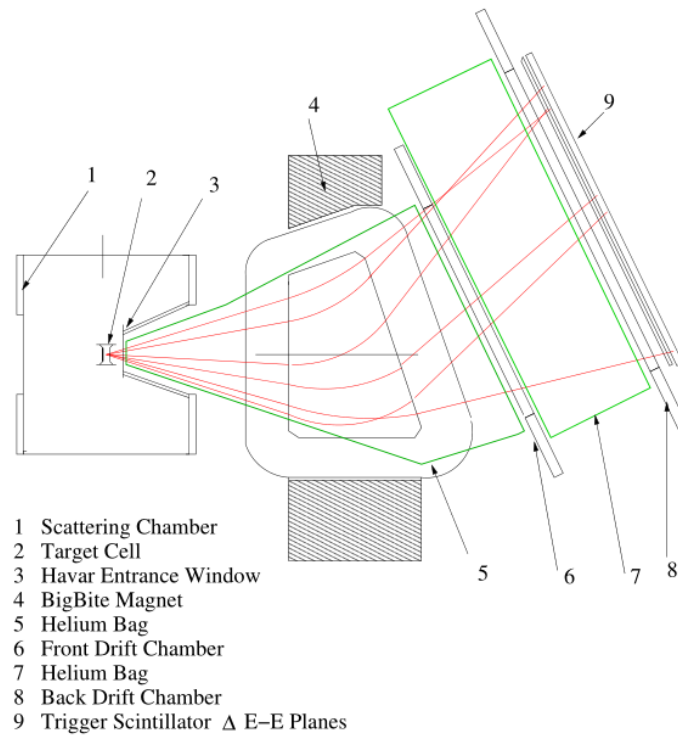


Figure 3.10: Layout of BigBite. Figure is from ref. [13].

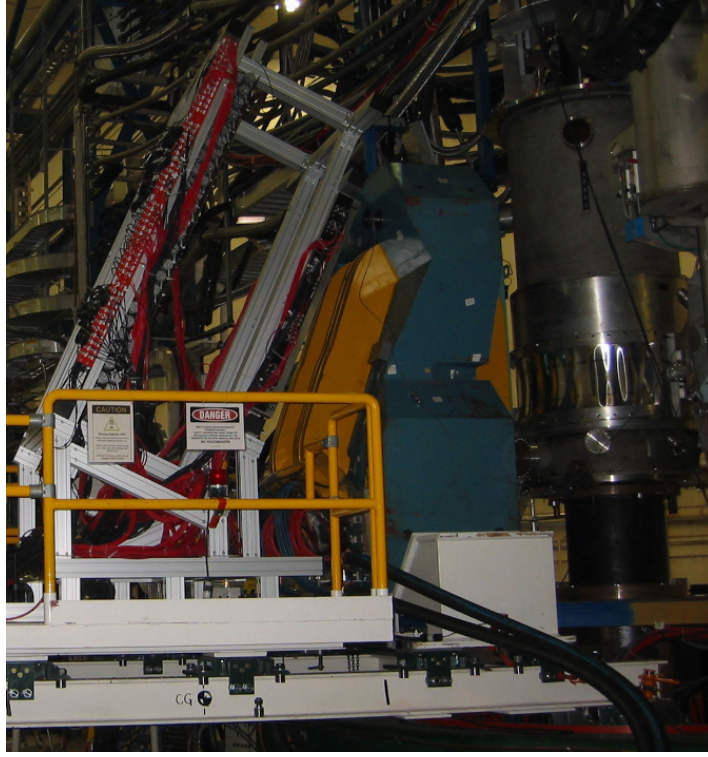


Figure 3.11: BigBite Magnet and structure holding MWDCs and scintillators.

3.4 Trigger

The coincidence trigger was formed by S2 scintillator plane in the Left HRS and either the E or dE scintillator plane in the BigBite. All triggers including BigBite dE trigger, BigBite E trigger, Left HRS S2 trigger, coincidence trigger and electronic pulser (random trigger) were sent to the trigger supervisor. The trigger supervisor recorded the triggers and selected which trigger initiated the electronic data recording process by sending out a signal to start the ADC and TDC gates in the readout electronics. The selection of various triggers was weighted by a prescale factor.

Table 3.2: Trigger

T_1	BigBite E-plane
T_2	BigBite dE-plane
T_3	L-HRS Singles
T_4	L-HRS Efficiency
T_5	$T_1.AND.T_7(\text{coincident})$
T_6	$T_2.AND.T_7(\text{coincident})$
T_7	L-HRS Singles (center S1 paddles.AND.S2)
T_8	1024 Hz pulser

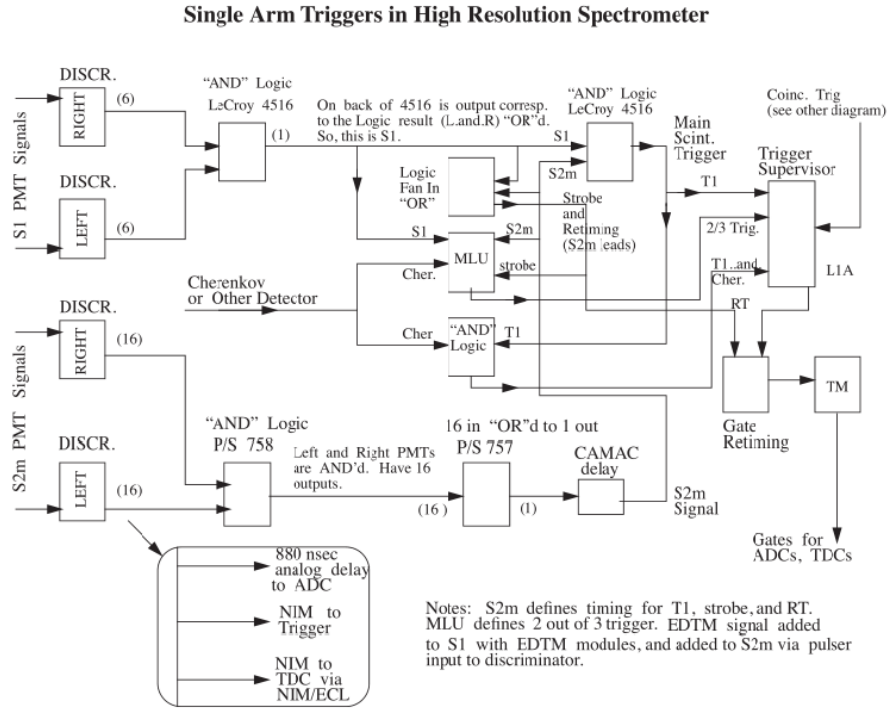


Figure 3.12: Trigger diagram for left HRS during E04-007. Figure is from R. Michaels,

<http://hallaweb.jlab.org/equipment/daq/strig.ps>

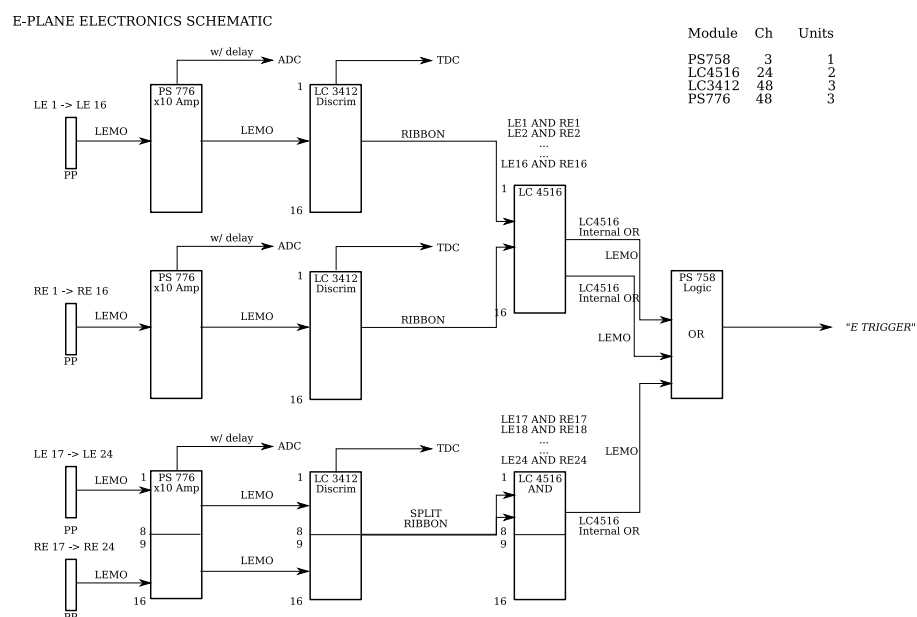


Figure 3.13: Trigger diagram for BigBite E-plane. Figure is from B. Moffit,

https://userweb.jlab.org/~moffit/meetings/BigFamily/summer/E_electronics.pdf

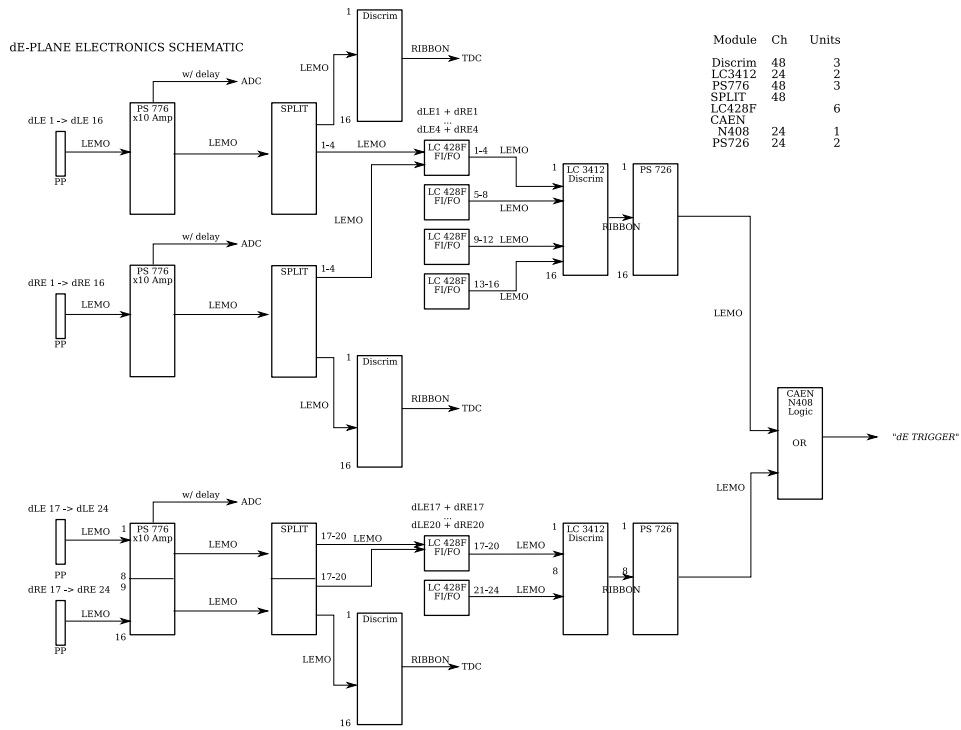


Figure 3.14: Trigger diagram for BigBite dE-plane. Figure is from B. Moffit,

https://userweb.jlab.org/~moffit/meetings/BigFamily/summer/deltaE_electronics.pdf

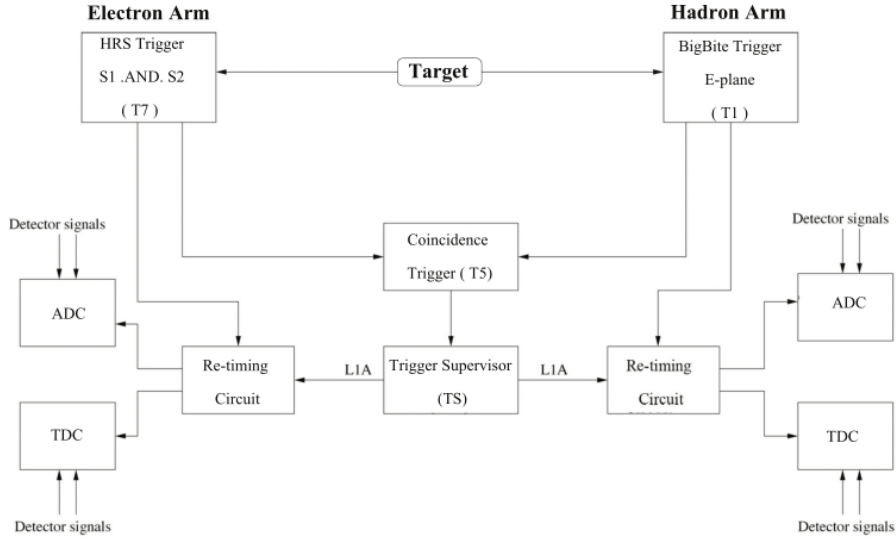


Figure 3.15: Diagram of coincidence trigger between the BigBite and left HRS. Figure is from ref. [21]

Table 3.3: Kinematic setup summary

beam energy(GeV)	$\theta_{BB}(deg)$	$\theta_{HRS}(deg)$
1.193	-54.0	35.5
		20.5
		16.5
		14.5
		12.5
	-48.0	27.0
		20.5
		16.5
		14.5
		12.5
	-43.5	20.5
		16.5
		14.5
2.323	-54.0	13.2
		15.8
		18.2

For more details on the apparatus and data acquisition please refer to ref. [21].

Chapter 4

Data Analysis

4.1 Calibration

4.1.1 Beam Energy

The beam energy, measured in an arc section of the beam line, was verified by using elastic scattering from various targets including hydrogen, deuterium, carbon and tantalum. Normally, the beam energy is kept constant (“locked”) by a feedback system which tightly constrain the the position of the beam before and after the arc. But, during the first 2 weeks of taking data, there was a problem with the energy lock provided by the accelerator, which resulted in a drifting of the beam energy by the order of 100 keV. This can result in a miscalibration of W and Q^2 in the acceptance. This effect was accounted for by using the real beam energy distributions (distributions of the most probable beam energy from each run weighted by accumulated charge) in the simulation.

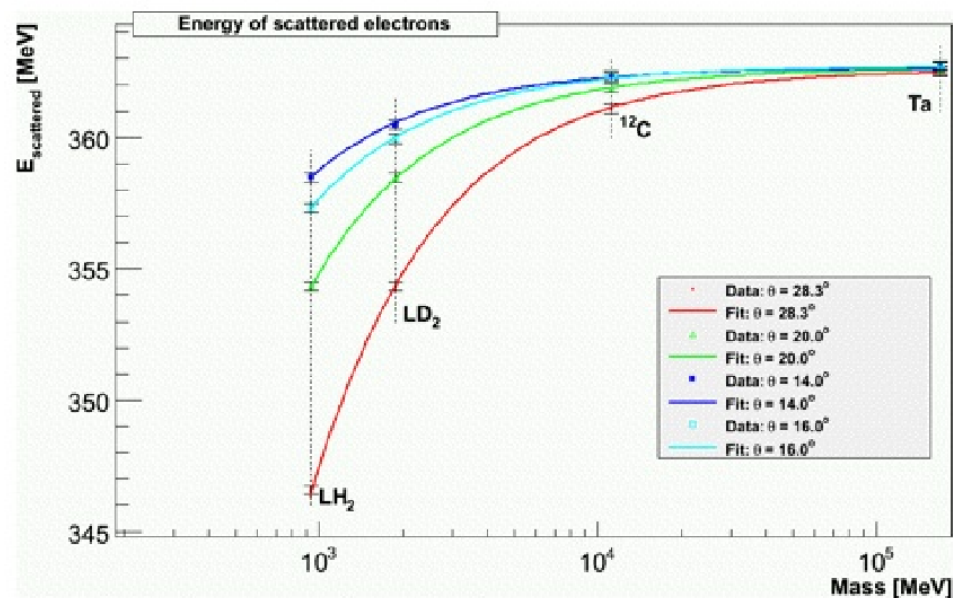


Figure 4.1: Beam energy determination by fitting the scattered electron energy measured in LHRS versus target mass, using elastic scattering from four different targets at various scattering angles ($E' = \frac{E}{1 + \frac{2E}{m} \sin^2 \frac{\theta_c}{2}}$). Figure is from ref. [36].

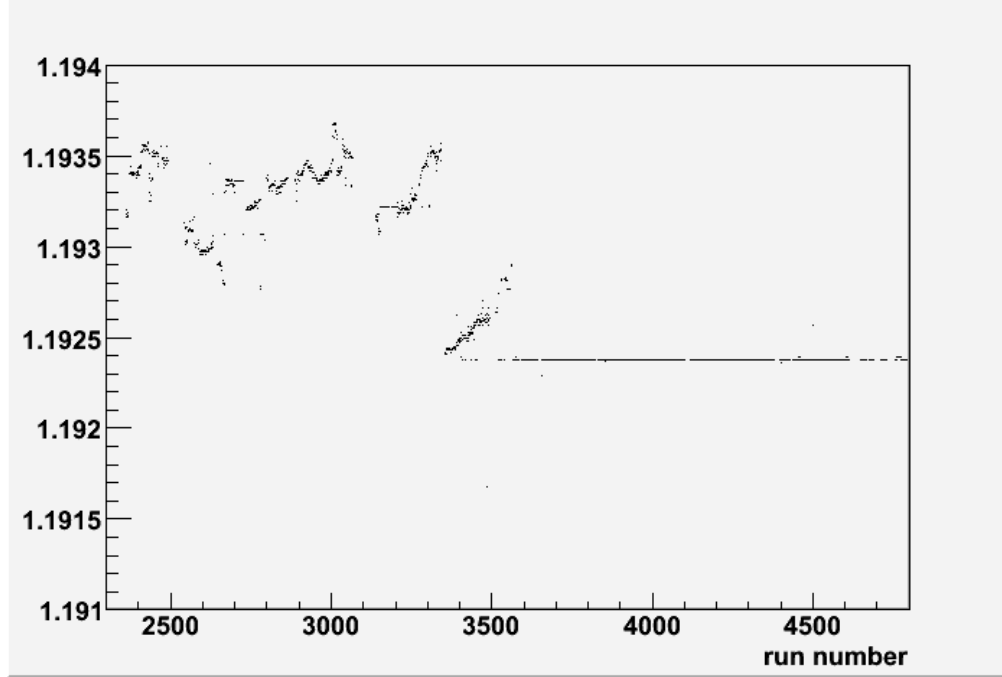


Figure 4.2: Plot of beam energy in GeV vs run number. The beam energy plotted here is the most probable beam energy for each run. This plot does not reflect the spread of the beam within the run. Runs after 3500 had the accelerator controlled energy lock, which stabilized the beam at 1192.38 MeV. The beam was then constantly adjusted (from beam energy read out feedback) to maintain this nominal value.

4.1.2 Electron Detection using Left HRS (LHRS)

In this experiment the electron was detected in the LHRS using the standard setup with S1, S2 and the VDCs. Particles other than electrons are excluded by the magnet field and time of flight information. The Gas Cerenkov was initially used for confirmation that an electron was detected, but not used in the analysis. The scattered electron in the LHRS

was detected in coincidence with the recoil proton in BigBite. The missing mass¹ spectrum was determined from the measured momentum vectors of the detected electron and proton and a peak in the missing mass spectrum at the π^0 mass determined whether or not a π^0 had been produced.

The Vertical Drift Chamber (VDC) calibration mainly involves extracting t_0 for each wire. This t_0 is basically the rising edge of the drift time distribution measured by the time-to-digital converter (TDC). Also, the TDC offsets of S1 and S2 were adjusted to center the TDC distribution of every scintillator paddle at the same channel. Since the electron travels essentially at the speed of light, the time it takes to travel to each paddle depends only on the path length. After the VDC calibration and S1, S2 calibration, the HRS transport optics are obtained from fitting polynomial expansions of the focal plane variables to data taken during calibration runs using sieve slits, a multi-foil target and elastic scattering from various targets. For details on calibration of the HRS optics refer to ref. [32] and [37].

¹From the reaction $e^- + H \rightarrow e' + p + \pi^0$ written in terms of 4 momentum $k + p = k' + p' + p_{\pi^0}$, the missing mass is defined by $(k - k') + (p - p') = p_{\pi^0}$. Square both sides $((k - k') + (p - p'))^2 = (p_{\pi^0})^2 = m_{\pi^0}^2$. So missing mass equals m_{π^0} indicate that π^0 is produced.

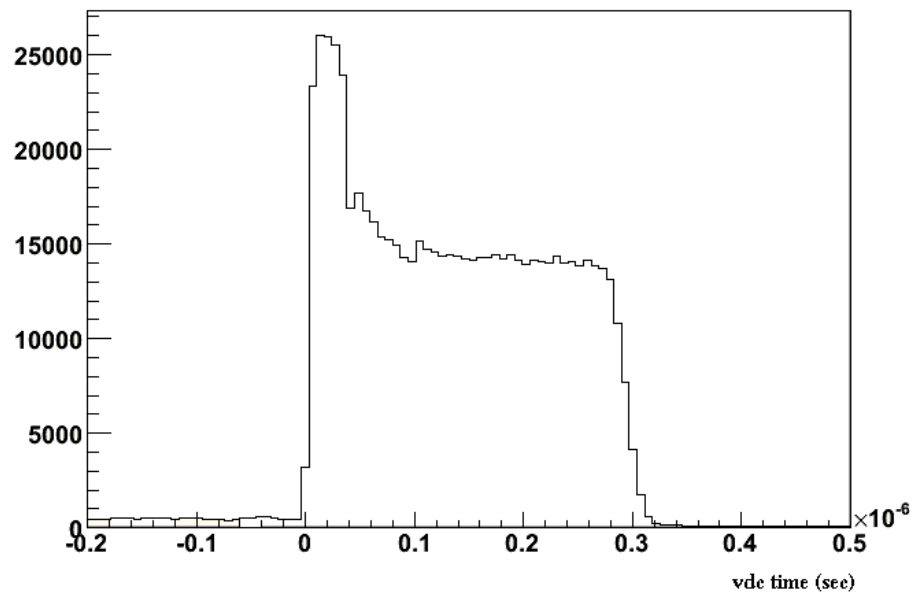


Figure 4.3: The VDC time spectra of the wire number 200 of the first wire plane of the first VDC after t_0 calibration.

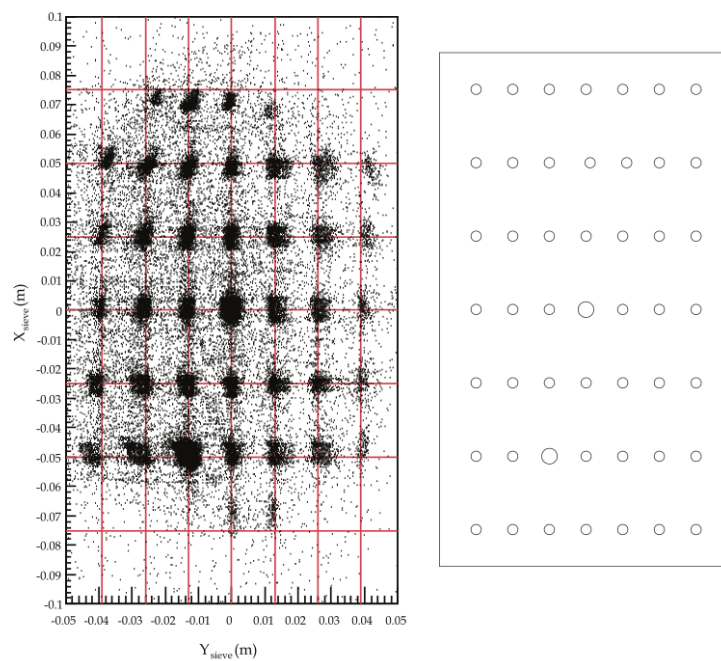


Figure 4.4: Left: HRS sieve pattern from the LH2 target. The central momentum for the LHRS was set to 0.9654 GeV/c at a scattering angle 35.5° . Right: Sieve hole geometry. Figure is from ref. [21].

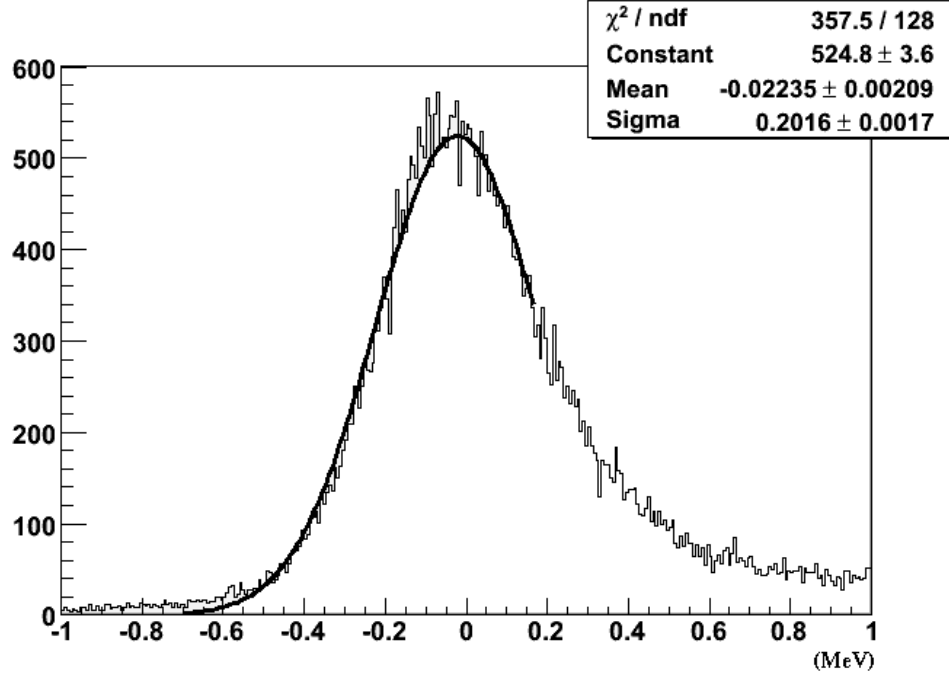


Figure 4.5: $w - w_{Ta}$ spectra of Ta target, where $W_{Ta}=168,551.1876$ MeV is the mass of Ta.

4.1.3 Proton Detection using BigBite

4.1.3.1 BigBite ADC

The high voltages for PMTs were adjusted to equalize the ADC response from each PMT, as shown in Figure 4.6. The thick (E) and thin (dE) scintillators in BigBite were designed to be used for trigger and particle identification (PID). ADC values were used as PID during calibration (especially in determination of MWDC tracking efficiency), but were not used as a cut while extracting cross sections, as other particles were already practically excluded by time-of-flight and missing mass cuts. In addition, signal thresholds in the BigBite triggers (signal from E and dE scintillators) were set to suppress pions, which deposited significantly less energy in the scintillators compared to the low momentum protons.

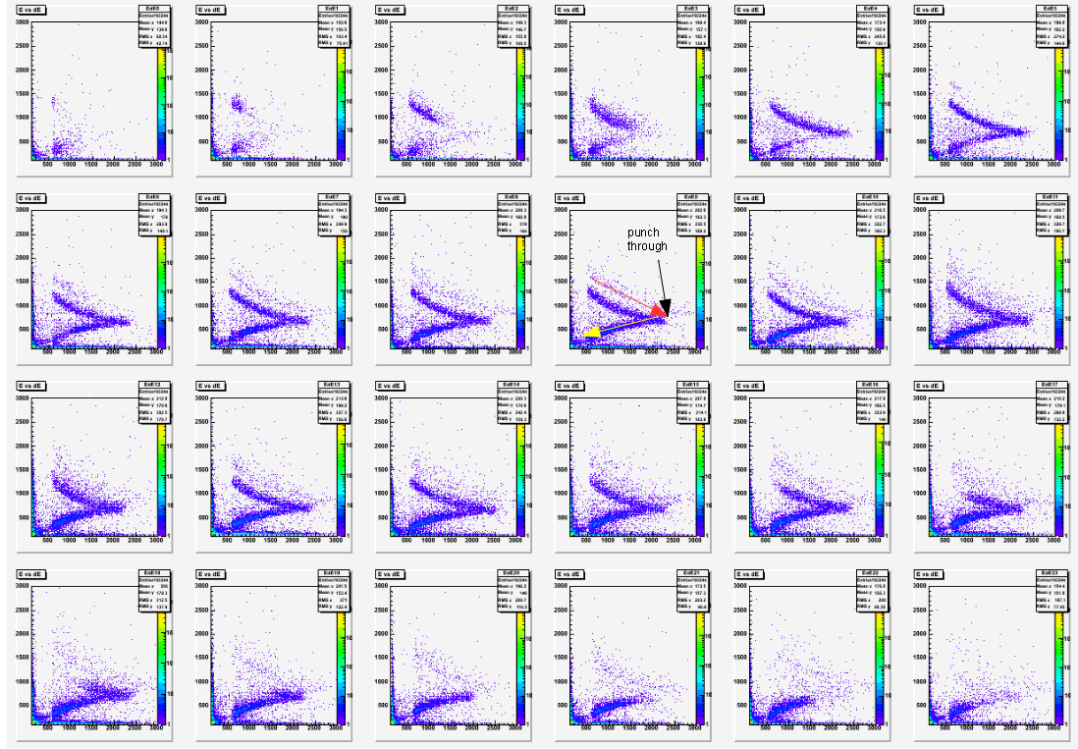


Figure 4.6: Plot of BigBite E ADC (x-axis) versus dE ADC (y-axis) of all 24 E bars and 24 dE bars; the units are channels. Considering the middle plot, as particle energy increases, less energy is deposited in the dE, while particles stop in the E bar deposit all their energy, i.e., dE ADC signals go down and E ADC signals go up (in red arrow direction). At the point where particles have enough energy to go through E bar (punch through), the energy deposited goes down as the particle energy increases (in the yellow arrow direction). Punch through points in each bars happened at about the same point, as shown in the plots, indicating well calibrated PMTs (ADCs).

4.1.3.2 BigBite TDC

Time walk is the deviation in the measured time of a PMT signal caused by the varying amplitude of the signal. Given a fixed rise time, a higher amplitude signal will cross the

discriminator threshold sooner. For the BigBite thick E scintillators, this time walk can be up to 3 ns, so a correction following the standard form $tdc_{corrected} = tdc_{measured} - \frac{w}{\sqrt{(ADC - pedestal)}}$ was applied, where the factor w was obtained empirically for each PMT. After the time walk correction was applied, TDC offsets were obtained to align the TOF peaks in each paddle. Because the gap between the 30 mm and the 3mm thick E and ΔE scintillators in BigBite is of the order of 1 cm, the time it takes the proton to pass through the gap is of the order of 0.10 - 0.16 ns for 20 - 50 MeV protons. The TDC offsets were set so the measured times are about the same for each E and ΔE pair.

4.1.3.3 BigBite Wire Chamber

The t_0 drift time calibration procedure is similar to that of the LHRS VDCs. The drift time between the interaction point and the wire is determined from known drift velocities and fitted time constants and is converted to a distance between the interaction point and the wire which later is used to find a track. The time-to-distance conversion is obtained by fitting a relationship between the drift time and the drift distance from reconstructed tracks. The difference between the distance obtained from converting the drift time and the distance obtained from the reconstructed track is called the residual. The smaller the residual the more reliable the track and the more accurate the conversion function. The residual and tracking are improved by repeated fitting of t_0 and the conversion function. As t_0 and the conversion function get better, the tracking gets more accurate. Using more accurate tracks to fit t_0 and conversion function result in more accurate t_0 and conversion function.

The BigBite tracking software was developed by O. Hansen. The Pattern Match Tree Search algorithm [38] essentially generates templates of the hit pattern and then matches the

hit information to these patterns using a recursive procedure which progressively increases the search resolution. For more information about the calibration of BigBite Wire Chamber and tracking software, please refer to ref. [35].

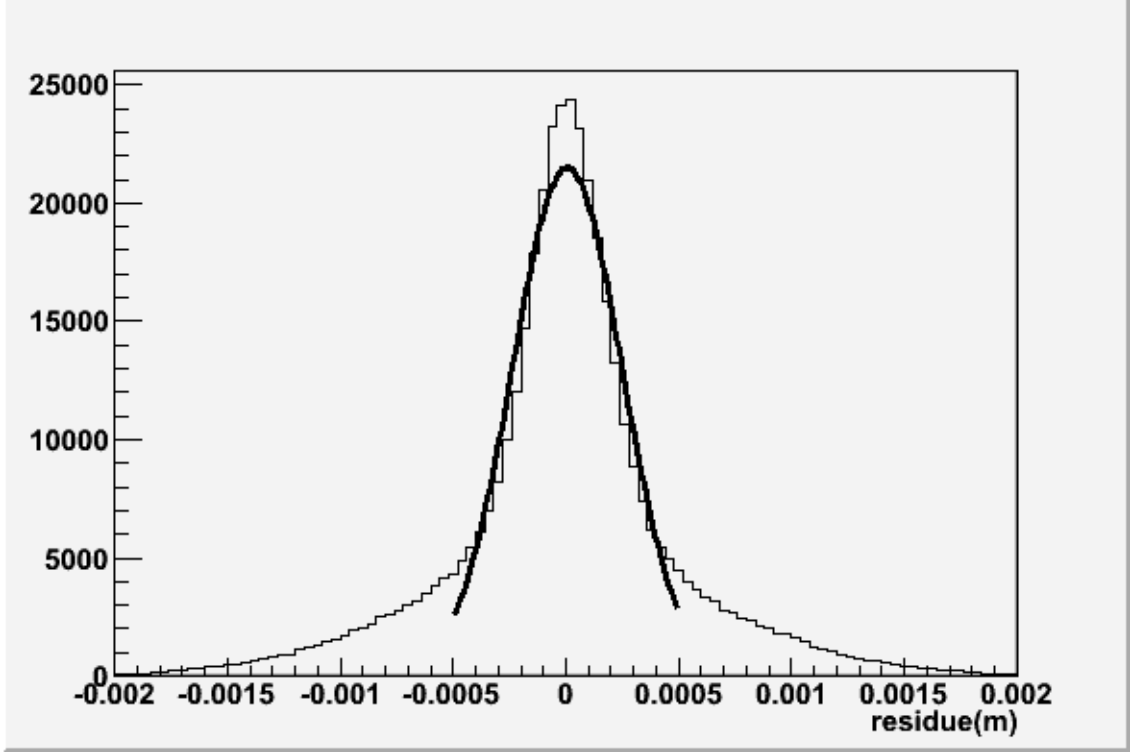


Figure 4.7: MWDC first plane residue (difference between track position and hit position) spectrum after calibration. The big tail spread on both sides came from accidental background. The uncalibrated t_0 would result in a wider spread and asymmetric shape of the residue. The sigma from fitting is 2.43×10^{-4} .

4.1.3.4 BigBite Optics

The track information in the MWDC has to be converted to proton momentum and angle at the reaction vertex in the liquid hydrogen target. In lowest order it is first assumed that the BigBite magnet is a perfect, uniform dipole with strength B in a finite volume. In

that case the proton momentum is given by $p = 0.3 \times B \times R$, where R is the bend radius in Figure 4.5. To find R , the midplane approximation is used as described below.

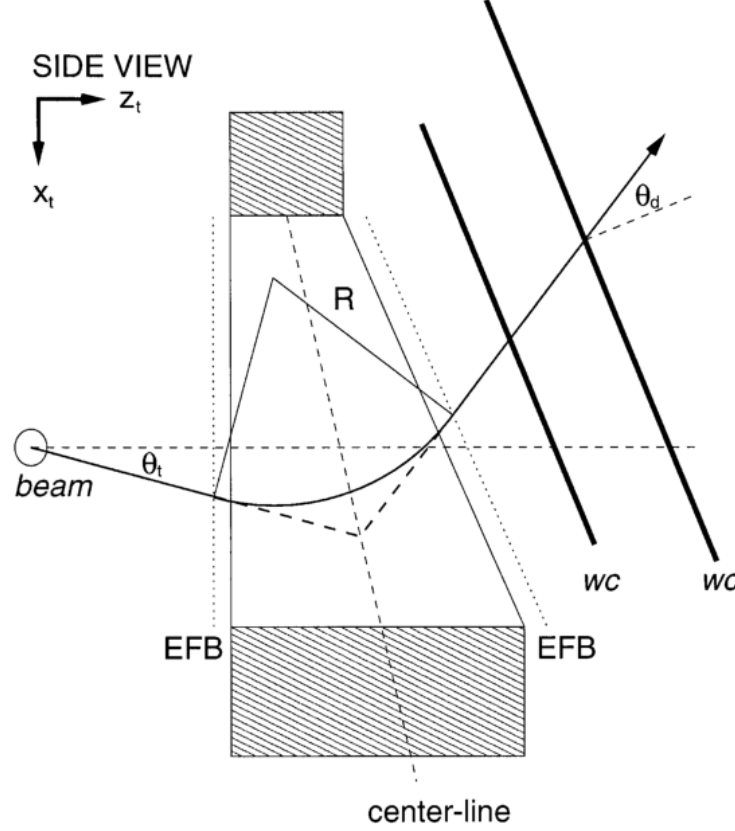


Figure 4.8: View of the dispersive plane of the BigBite spectrometer. The dotted lines labelled EFB indicate the effective field boundaries. The position of MWDCs is indicated by WC. The figure is from ref. [33]

The track is projected from the MWDCs back to the mid plane of the magnet, which is shown as the center line in Figure 4.8. By requiring that the proton came from the target, the part of the track from the target to this mid plane is determined at the intersection point. The first part of this track is then adjusted so that the whole track behaves like it is

going through a pure dipole so that the momentum is proportional to the arc of the curve, or equivalently, the radius R . To do this, the positions of the MWDCs and magnet are needed. The MWDC positions were first set according to the survey report. The survey report gives approximately where the center of the 1st MWDC is and the distance between the front and rear MWDC. This center position was moved in that plane so that the tracks from zero-field calibration runs point back to target. The distance between the front and rear chambers were determined by moving one chamber in and out from its nominal position, to minimize the residuals. The hydrogen elastic data were used as a starting point to locate the center and boundaries of the magnet field. Using the LHRS to measure the momentum and angle of the electron scattered elastically from the hydrogen target, the angle and momentum of the scattered proton is known from the kinematics of the scattered electron. The position of the dipole magnet was adjusted so that the direction of the proton momentum agreed with what was expected from the detected electron.

These data only determined the optics for a small region of the of MWDC since for elastic scattering, only a small cone of coincident protons pass through BigBite due to the small acceptance of the LHRS. To extend the optics to the entire region of MWDC, other information from the $p\pi^0$ reaction has to be used. For unpolarized beam and target, the cross section has to be symmetric above and below the momentum transfer vector \vec{q} . For a small bin of center of mass energy ΔW near threshold, a small cone of protons is produced around \vec{q} with a symmetric distribution above and below. This distribution covers most of the MWDC. The MWDC position is then changed slightly until the proton distribution is appropriately centered around \vec{q} .

At the edges of the magnet, fringing effects introduce vertical components to the B

field causing slight bending in the horizontal direction. This can lead to mis-reconstruction of the horizontal angle and vertex position at the target and can create distortions in the acceptance. To correct this, the vertex reconstructed from BigBite and the vertex reconstructed from the LHRS are compared.

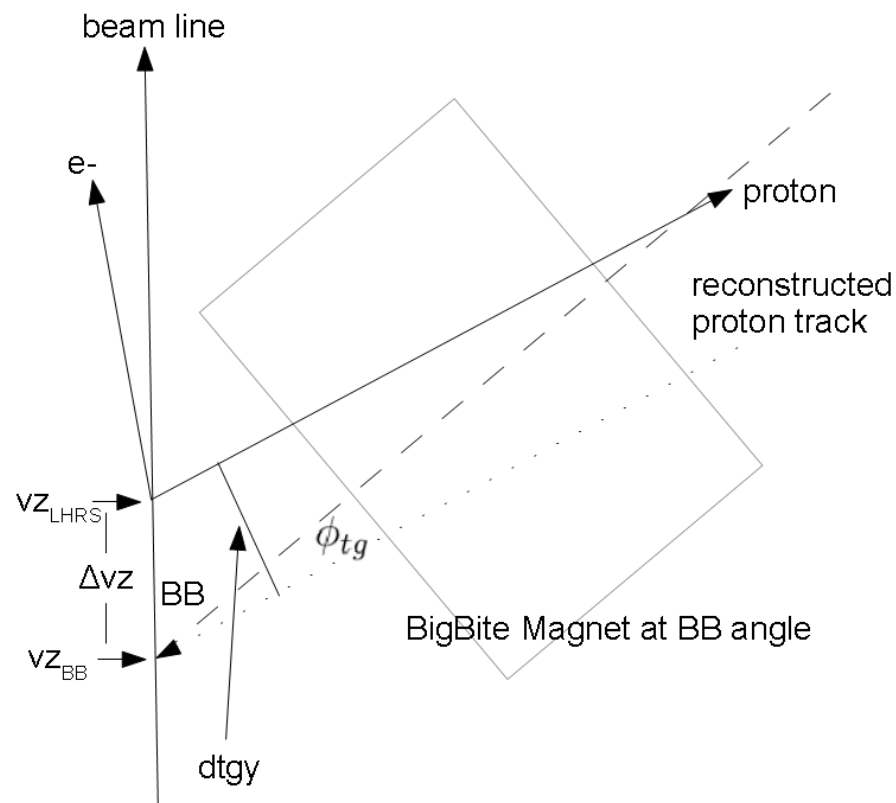


Figure 4.9: The dotted line is the proton track before ϕ the correction. The dashed line is normal to the BigBite magnet.

From figure 4.9

$$\Delta vz = vz_{LHRS} - vz_{BB} \quad (4.1)$$

$$dtgy = \Delta vz \cdot \sin(BB + \phi_{tg}) \quad (4.2)$$

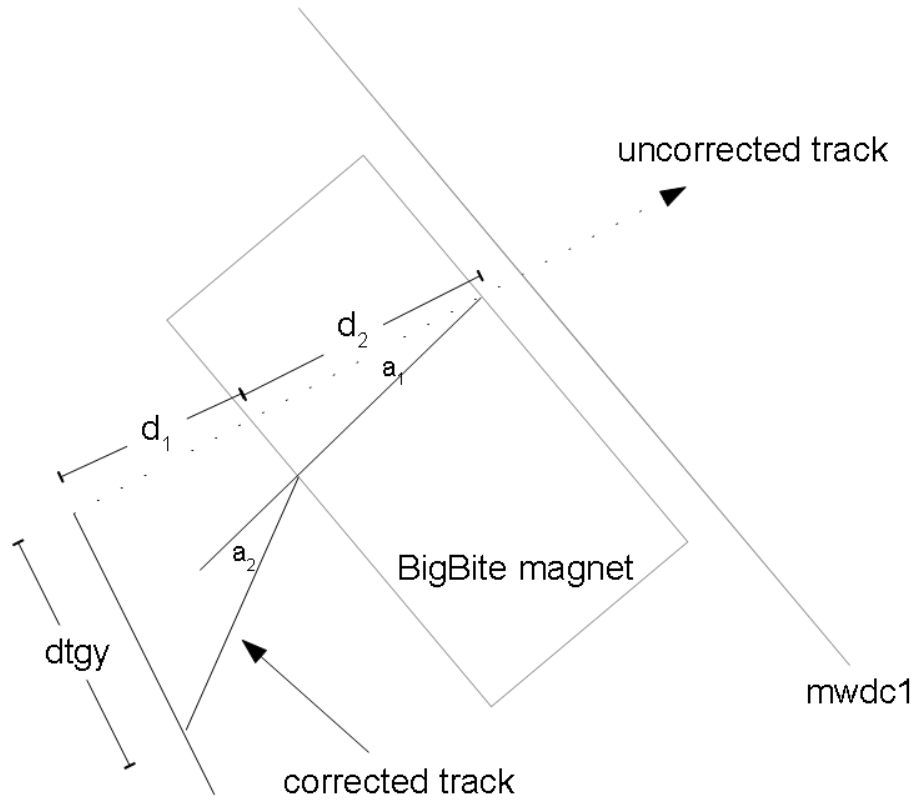


Figure 4.10: The proton track before and after ϕ correction. d_1 is the distance in the horizontal plane before the proton enters the BigBite magnet. d_2 is the distance in the horizontal plane inside the BigBite magnetic field.

In figure 4.10, assuming the BigBite magnet is a dipole in the vertical direction, then

a_1 and a_2 are equal.

$$dtgy = 2d_1 \tan(2a_1) + d_2 \tan(a_1) \quad (4.3)$$

and since this a_1 is very small

$$dtgy = 2d_1 2a_1 + d_2 a_1 \quad (4.4)$$

From equation (4.2) and (4.4), the correction for ϕ

$$2a_1 = \frac{2\Delta vz \cdot \sin(BB + \phi_{tg})}{2d_1 + d_2} \quad (4.5)$$

After the ϕ correction, the π^0 missing mass was fitted by adding the correction terms to proton momentum (also using the energy loss correction from Bethe-Bloch formula given in Ref. [39] in the calculation). By adding the correction term to ϕ and momentum, the fringe field is now accounted for in the calculation.

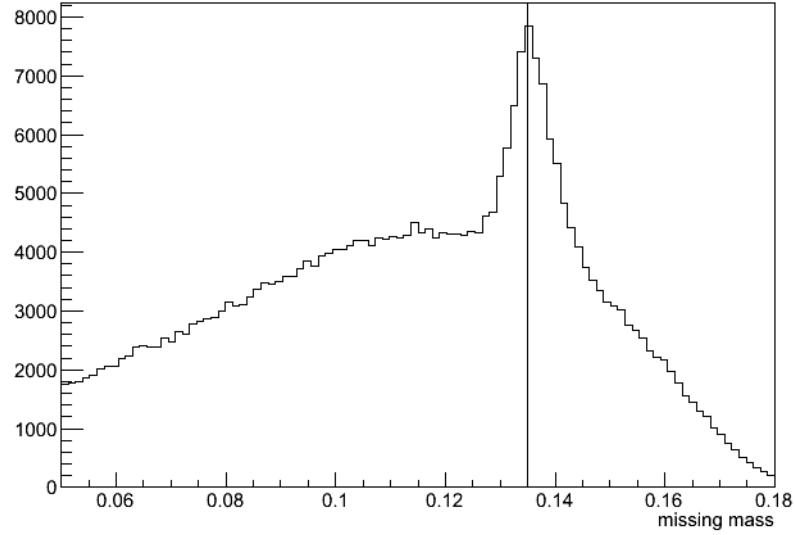


Figure 4.11: Missing mass spectrum before accidentals background subtraction. π^0 mass is $0.135 \text{ GeV}/c^2$ indicated by the vertical line.

4.1.4 Time of Flight

Due to the way the coincidence trigger was set up, T_3 (LHRS S2) was timed using BigBite timing $BB_{time} = (BB_{left\ time} + BB_{right\ time})/2$ as a common stop. So the electronic timing is $0.5 \times T_3 + BB_{time} - LHRS_{time}$, where 0.5 is the resolution of T_3 . This has to equal the physical proton time of flight p_{tof} - electron time of flight e_{tof} with some offset. The final quantity used to make cuts was $tof = p_{tof} - e_{tof} - (0.5 \times T_3 - LHRS_{time} + BB_{time}) + offset$. Once the offset is determined, this distribution should be centered at zero.

The dE bar and E bar timing have different offsets, so they had to be determined separately. The tof quantity was calculated from either the E bar or dE bar, whichever gave a timing residual closer to zero.

$$tof = p_{tof} - e_{tof} - (0.5 \times T_3 - LHR S_{time} + BB_{ebartime}) + e_{offset}$$

or

$$tof = p_{tof} - e_{tof} - (0.5 \times T_3 - LHR S_{time} + BB_{debartime}) + de_{offset}$$

Lastly, other offsets were added to each S2 and each BigBite scintillator so that the *tof* had no dependence on scintillator. This made the *tof* peak narrower, thereby reducing the background under the peak and, consequently the systematic error associated with background subtraction.

Due to the larger attenuation of the light in the thinner dE scintillator paddles, sometimes the proton energy loss was insufficient to trigger the PMTs on both the left and right ends of the paddle. Using TDCs from only one side was not practical since only the mean time $BB_{time} = (BB_{left\ time} + BB_{right\ time})/2$ can give useful timing information. In this case, the *tof* was estimated from the proton momentum and pathlength through BigBite. In this case, the resolution is not as good.

$$tof = p_{tof} - e_{tof} - (0.5 \times T_3 - LHR S_{time}) + offset$$

After *tof* is calibrated, the background from out of time events can be subtracted off easily. The missing mass spectrum is much better in figure 4.15.

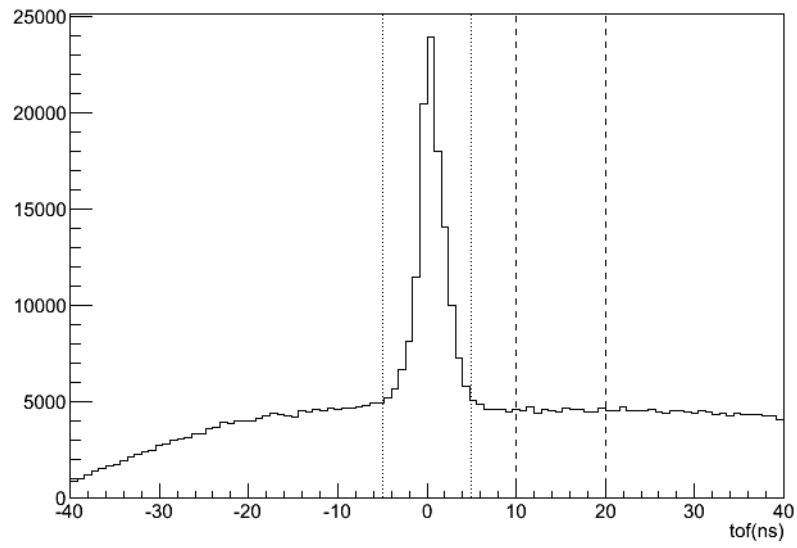


Figure 4.12: Time of flight spectrum. Dotted lines denote the coincident time window(-5 to 5 ns); dashed lines denote the out of coincident time window(10 to 20 ns) used for background subtraction.

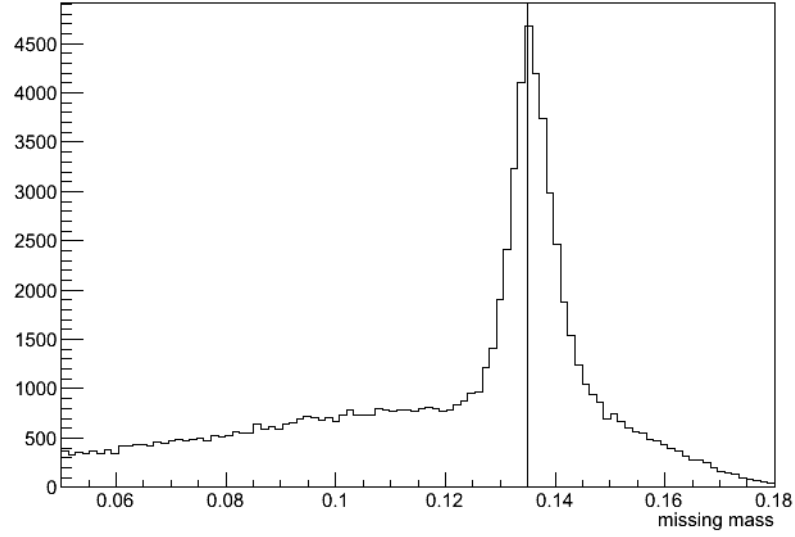


Figure 4.13: Missing mass spectrum corresponding to the events in the coincident time window shown in figure 4.12. Mass of π^0 is $0.135 \text{ GeV}/c^2$ indicated by the vertical line.

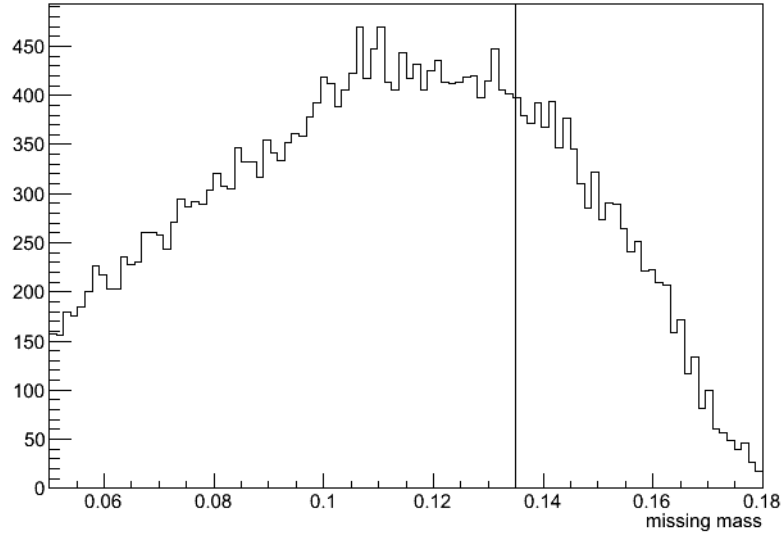


Figure 4.14: Missing mass spectrum corresponding to the events in out of the coincident time window shown in figure 4.12). Mass of π^0 is $0.135 \text{ GeV}/c^2$ indicated by the vertical line.

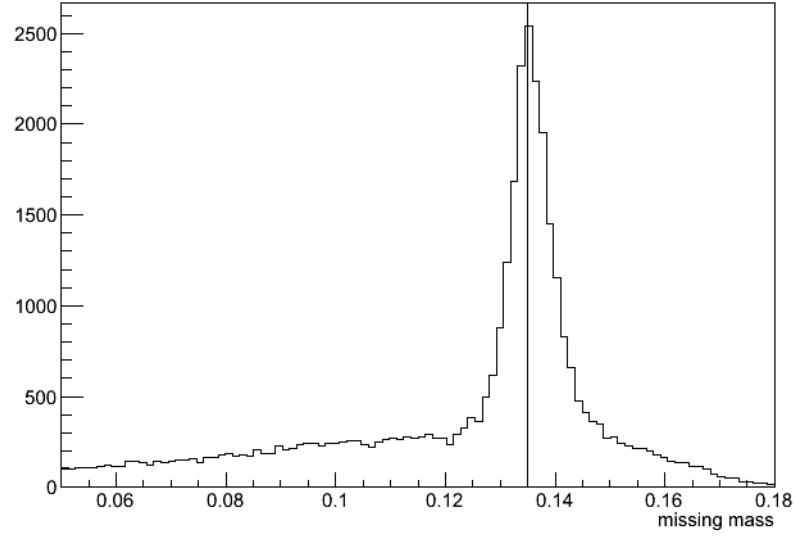


Figure 4.15: Missing mass spectrum after tof accidentals background subtraction, the spectrum in figure 4.13 minus the spectrum in figure 4.14. Mass of π^0 is $0.135 \text{ GeV}/c^2$ indicated by the vertical line.

4.2 Efficiency

4.2.1 BigBite MWDC Track Finding Efficiency

Several methods could be used to measure the track reconstruction efficiency:

1) Use elastic scattering in LHRS to kinematically force a proton into BigBite, thus insuring a proton for every elastic event.

2) Use $E - \Delta E$ cuts on the BigBite TOF paddles to select proton events.

Method 1) could not be used with the coincidence trigger as the ADC scintillator thresholds largely exclude proton momenta $> 500 \text{ MeV}/c$. Singles triggers could be used but this was not done. Method 2) was used by selecting a region in the $E - \Delta E$ spectrum where it

was known from missing mass cuts that the protons came from π^0 production. Then, events from this region were used to calculate the overall MWDC efficiency. Random backgrounds in the TOF paddles, which can dilute the efficiency calculation, were further reduced by using LHRS-BigBite coincidence TOF cuts.

4.2.2 BigBite MWDC Plane Hit Efficiency

To determine the intrinsic MWDC plane hit efficiency the redundancy of the MWDC tracking planes was exploited, along with the knowledge that at least one plane of each pair had to be used to generate the track. This method requires only the MWDC data itself, by selecting a wire hit n in one plane (e.g. U) associated with a known track, and checking the $(n - 1), n$ or $(n + 1)$ wire in the adjacent plane (e.g.- U'). This method assumes all the wires in the same plane have the same efficiency.

4.2.3 LHRS VDC,TDC and tracking

VDCs are used to generate tracks in LHRS. If every VDC has a hit, there should be a track. If a track is not found, then it is a tracking inefficiency. In the HRS, there are 6 tracking planes: the S1 and S2 paddles, and the U1, U2, V1, and V2 VDC planes, which should all fire when the electron passes. By requiring hits in 5 paddles/planes, the efficiency of the other paddle/plane can be determined.

4.2.4 Dead Time and EDTM

Dead time can be obtained from the count of events in the Trigger Supervisor. The other way is by counting the missing Electronic Dead Time Monitor (EDTM) pulses. From the way the EDTM pulser was setup, pulses were sent to the LHRS TDC in sequential

order from S2(S1) paddles 1 to 6 and the cycle then repeated. Counting missing EDTM pulses was straightforward. EDTM measured the overall dead time. Figure 4.20 show the difference between the T5 dead time and EDTM dead time (T5 being one of the main coincidence triggers).

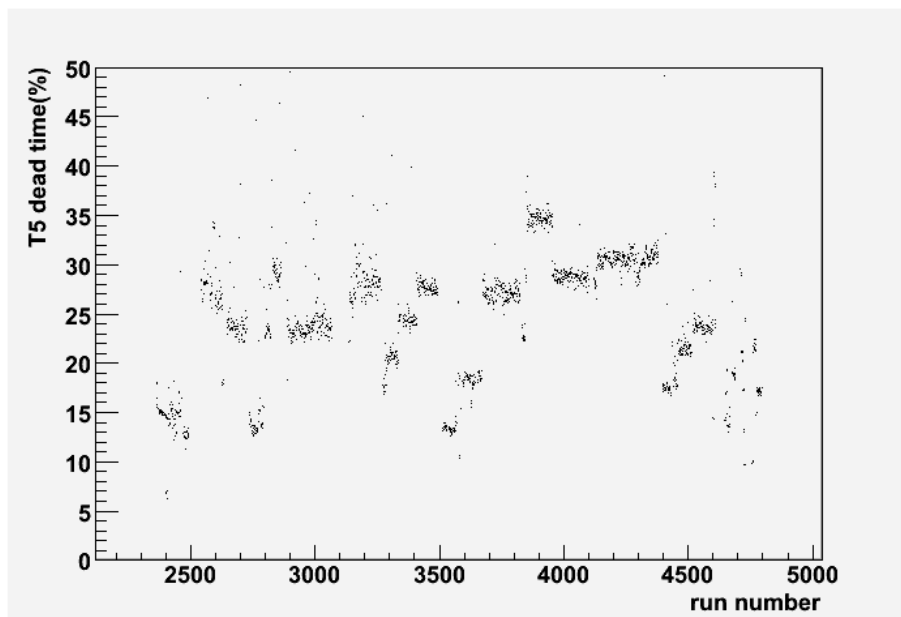


Figure 4.16: T5 dead time versus run number.

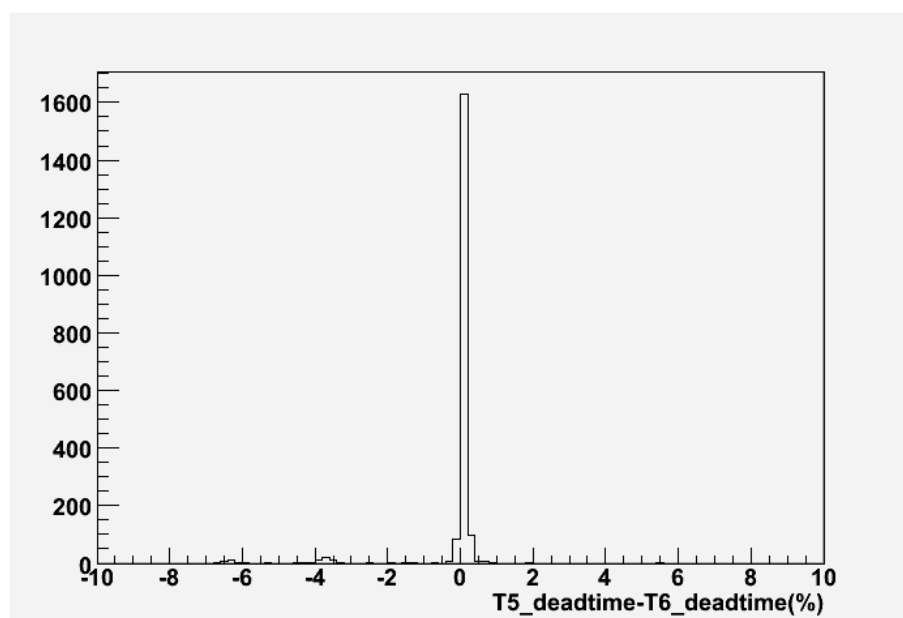


Figure 4.17: Difference between T5 dead time and T6 dead time (two main coincidence triggers).

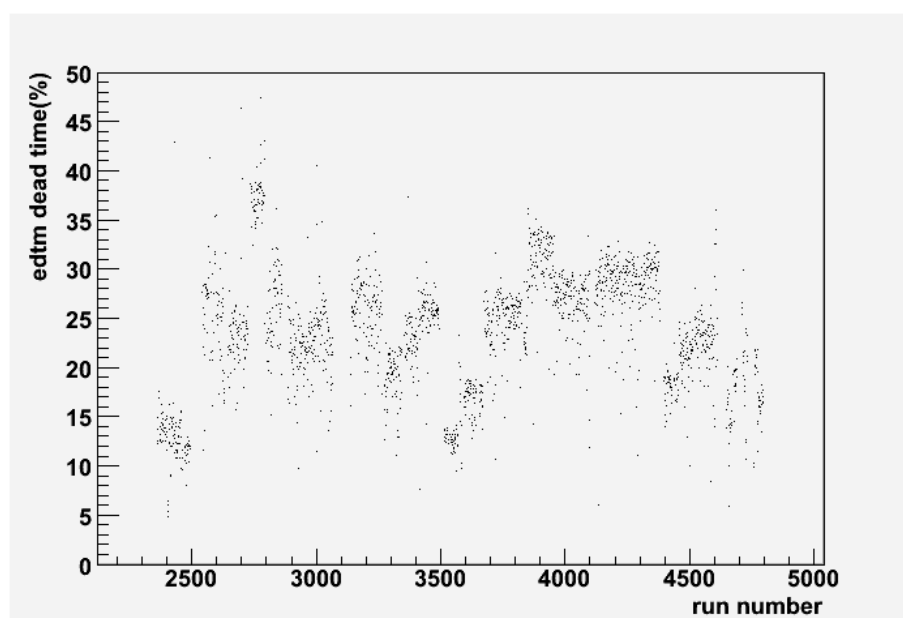


Figure 4.18: EDTM dead time versus run number.

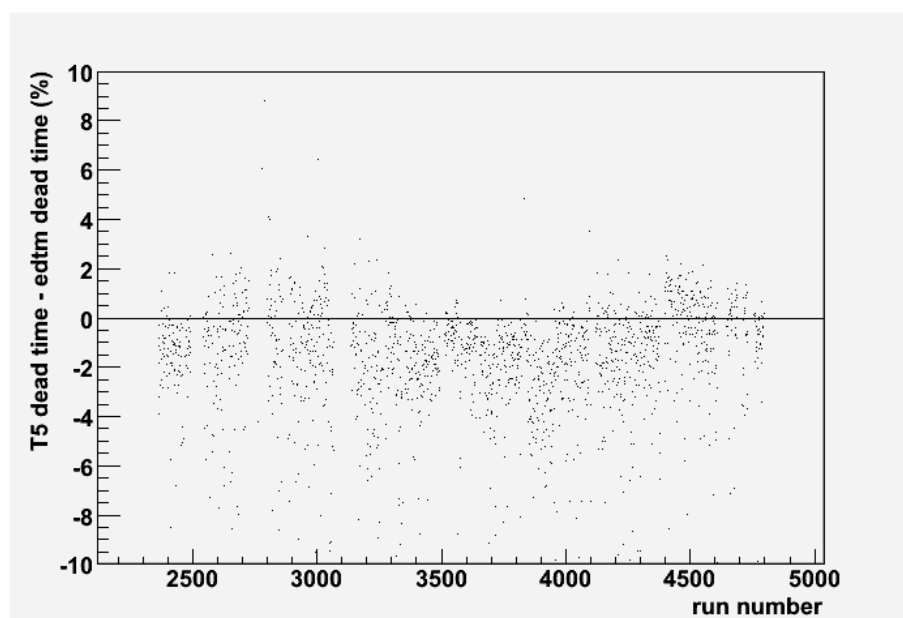


Figure 4.19: Difference between T5 dead time and EDTM dead time versus run number.

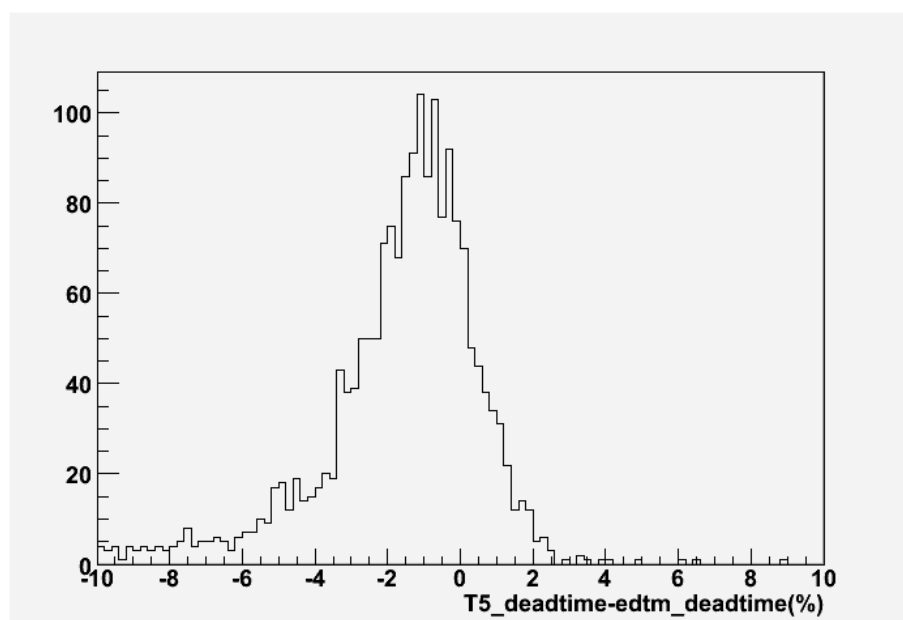


Figure 4.20: Difference between T5 dead time and EDTM dead time.

Table 4.1: Efficiency of run number 4760

LHRS VDC	0.9985
LHRS S2 TDC	0.9930
LHRS tracking	1.0
BigBite mwdc	0.9783
BigBite TDC	0.9770
BigBite tracking	0.8207
overall	0.7778

4.3 Simulation

The proton momenta associated with the π^0 production reaction extended to below 200 MeV/c at which point the LH2 target absorbed the protons. Protons in the lowest momentum ranges were subject to increasingly large multiple scattering and energy loss effects that had to be carefully simulated to account for their impact on the acceptance. The simulation on the BigBite side played a big role in this correction. The BigBite spectrometer, target chamber windows and LH2 cell were completely characterized in GEANT3. The magnetic field used in the simulation was generated using TOSCA by Vladimir Nelyubin based on NIKHEF drawings and measurements of the coil and field clamp dimensions. A physics event generator was used to simulate events statistically weighted according to the physics of the π^0 production reaction, using DMT [31] and MAID [30] models. A few checks were done to make sure that the simulation was consistent with data, mainly the hit positions and angles in the MWDC, which determined how accurately the Big Bite magnetic field, fringe fields and the MWDC positions in the simulation corresponded to the actual geometry.

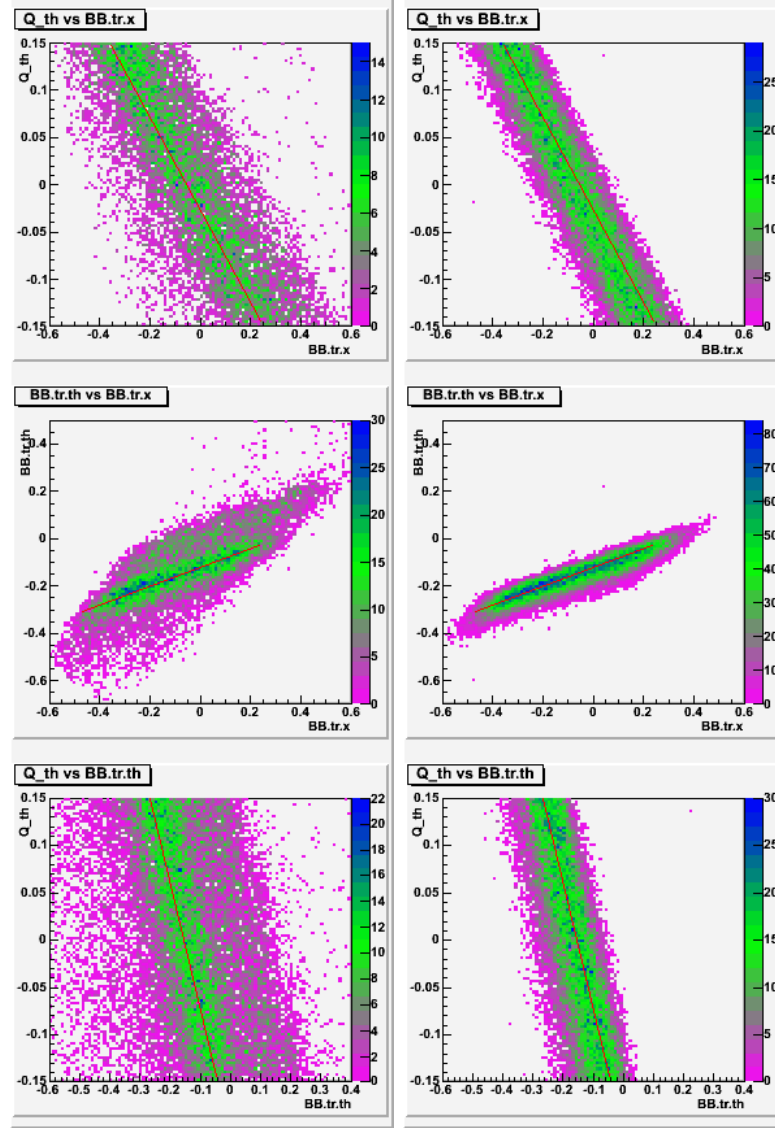


Figure 4.21: Left (right) show data (simulation) scatter plots. The red line, for reference, is at the same position in the left and right plots. Q_{th} is the \vec{q} vector vertical angle. $BB.tr.x$ is the vertical distance measured in meters in the first MWDC plane. $BB.tr.th$ is the track vertical angle at the detector.

The simulation was mainly used to provide the acceptance function, which is the number of reconstructed events in both LHRS and BigBite that passed the acceptance cuts, divided

by number of thrown events.

$$f_{acc} = \frac{N_{Reconstructed\ hits\ that\ pass\ all\ acceptance\ cut}}{N_{thrown\ events}} \quad (4.6)$$

It is always important to know where the acceptance of detectors fall off both in the data and in the simulation. The acceptance cut were used to avoid this fall off. The acceptance of LHRS and BigBite were obtained separately the same criteria. Since the spectrometers moved from setting to setting, it more suitable to define the acceptance in the Target Coordinate System (TCS) than in lab coordinate system. The TCS is the coordinate system center at the hall center and the z -axis lies along the central ray of the spectrometers. In the TCS, θ_{tg} is the vertical angle, ϕ_{tg} is the horizontal angle, p_0 is the central momentum setting in the spectrometer and y_{tg} is as defined in Figure 4.22. The acceptance depends most simply on θ_{tg} , ϕ_{tg} , dp/p_0 and y_{tg} . The cut on y_{tg} is taken care of separately in the vertex position vz cut. Making two dimensional plots of any of the target variable pairs will show most clearly where the acceptance drops off. Figure 4.25 shows the consistency of the data and simulation after applying the acceptance cuts to both. Plots similar to Figures 4.25, 4.27, 4.29 were carefully examined for any unphysical discrepancies between data and simulation.

After protons passed through all the material and were recorded as hits in the simulation, the tracks were reconstructed using the same optics as used for the data. For electrons, the GEANT3 simulation stopped at the entrance of the LHRS. Therefore, resolution effects of the LHRS consisted of smearing θ_{tg} , ϕ_{tg} , dp/p_0 based on the intrinsic resolutions in Ref. [32]. Both radiative and collisional energy losses of the incident and scattered electrons in the LH2 target cell and chamber windows, LH2, and LHRS entrance windows were simulated

in GEANT3. The energy losses were corrected in the simulated reconstructed data using the Bethe-Bloch formula given in Ref. [39] and applied the same way as to the real data. The simulation was also used to take care of many effects including finite resolution bin migration, beam energy drift and external radiation (straggling) in the target, that cannot directly be corrected for in the data. This was particularly important near threshold due to the rapidly rising cross section.

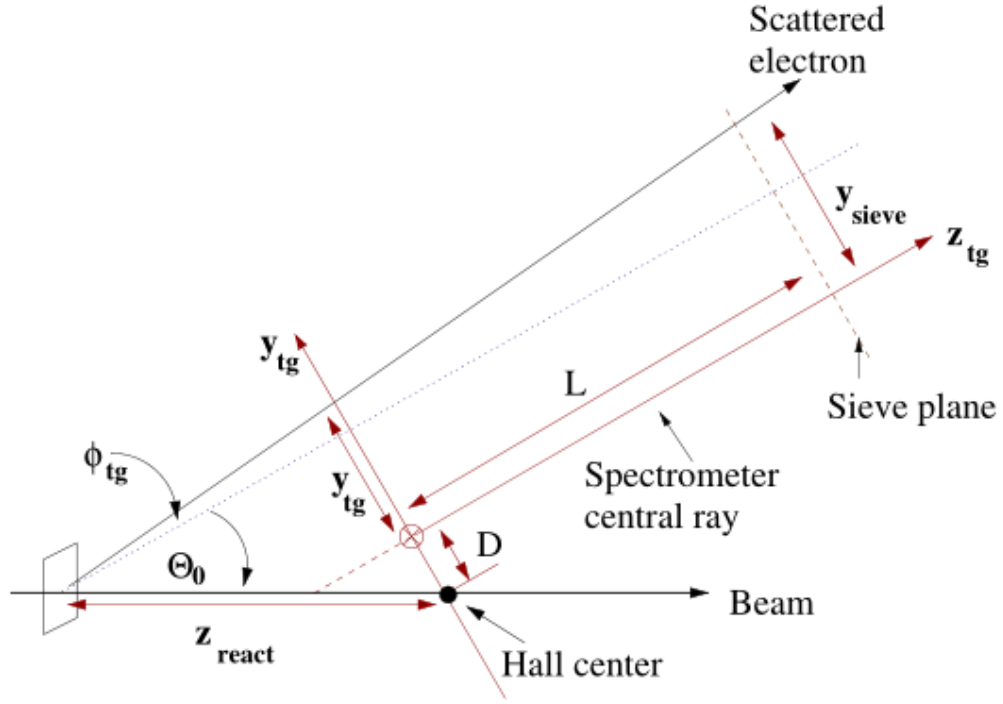


Figure 4.22: Target coordinate system (top view). Figure is from ref. [37]

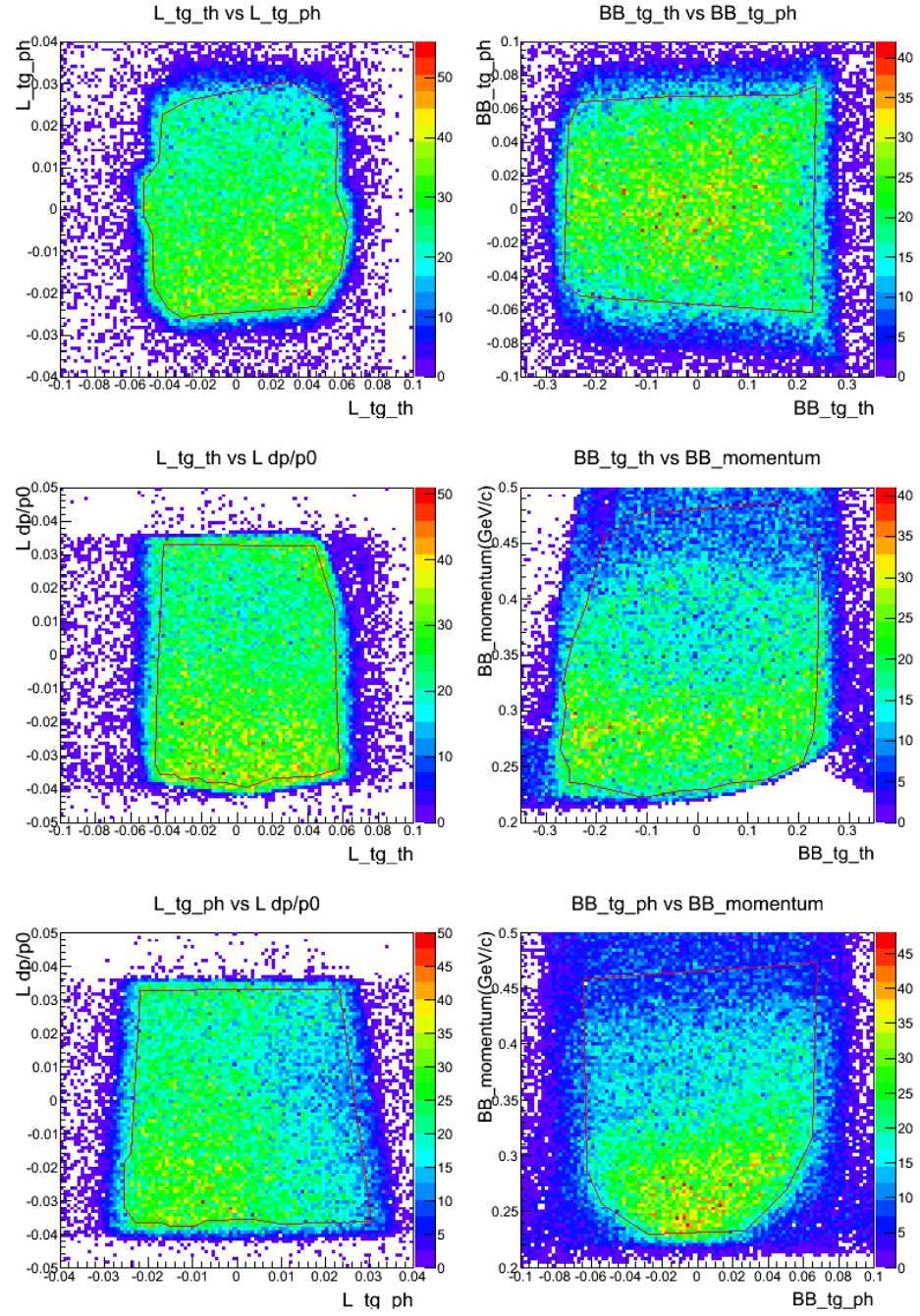


Figure 4.23: Reconstructed target variables from LHRs (left) and BigBite (right). Red lines are polygons used to define the acceptance cuts.

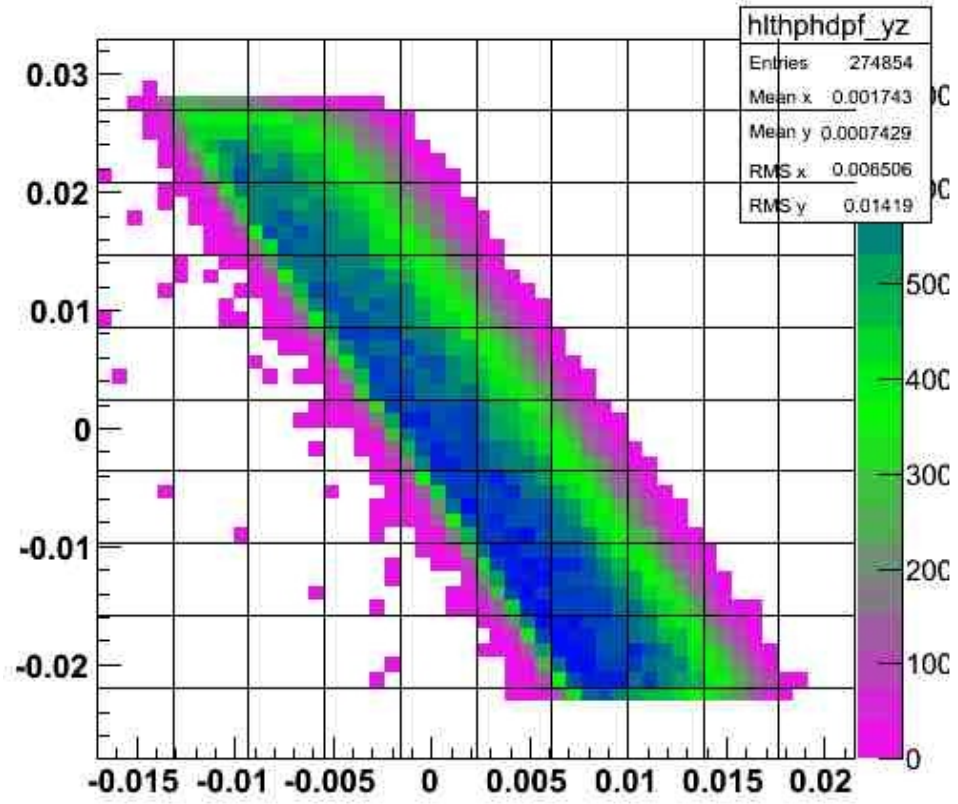


Figure 4.24: LHRs ϕ_{tg} (x-axis) versus dp/p_0 (y-axis) after applying the acceptance cut from Figure 4.23. An additional cut on the π^0 missing mass of $\pm 10 \text{ MeV}$ was applied to minimize contributions from the aluminum target cell windows.

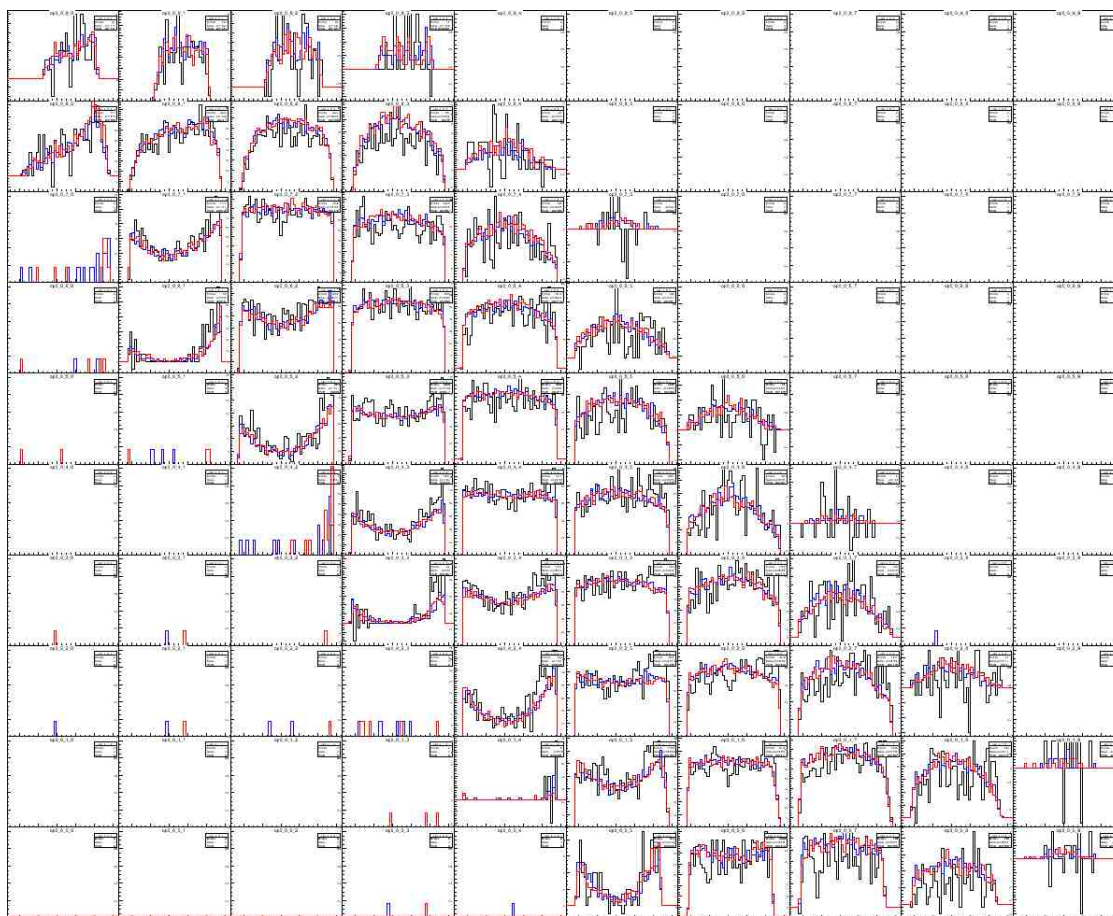


Figure 4.25: Each panel shows a comparison of data and simulation for the LHRs θ_{tg} distribution (black-data, blue-DMT, red-MAID). Each plot is positioned according to the value of ϕ_{tg} and dp/p_0 in the grid shown in Figure 4.24.

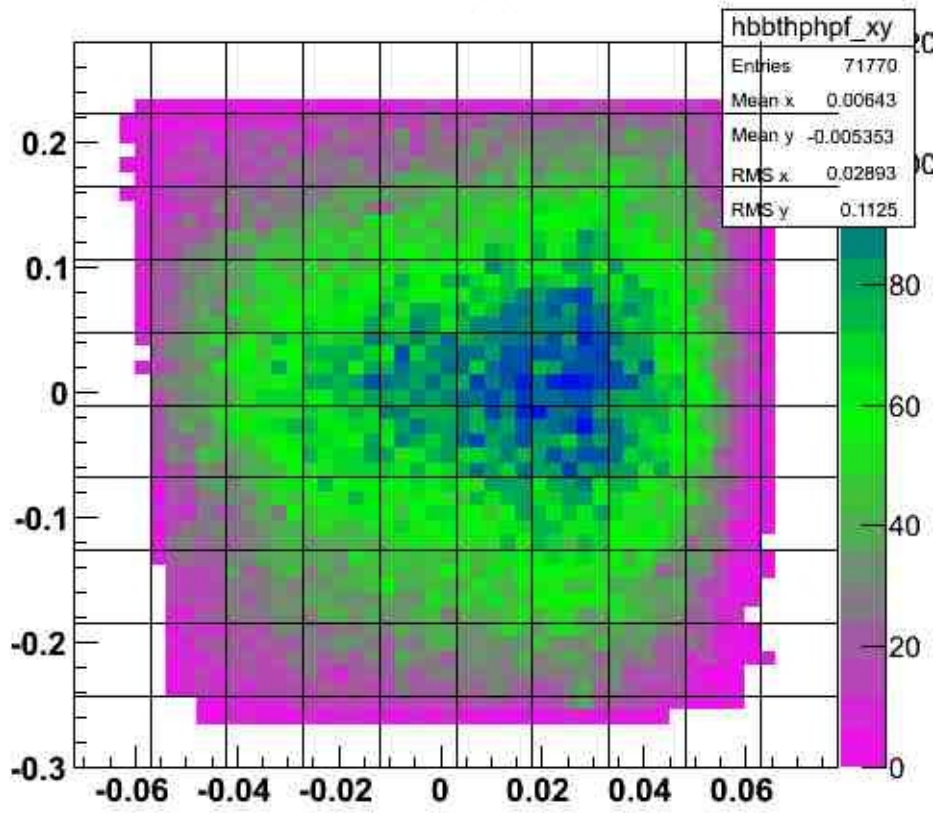


Figure 4.26: BigBite ϕ_{tg} (x-axis) versus θ_{tg} (y-axis). Cuts are the same as used in Figure 4.24.

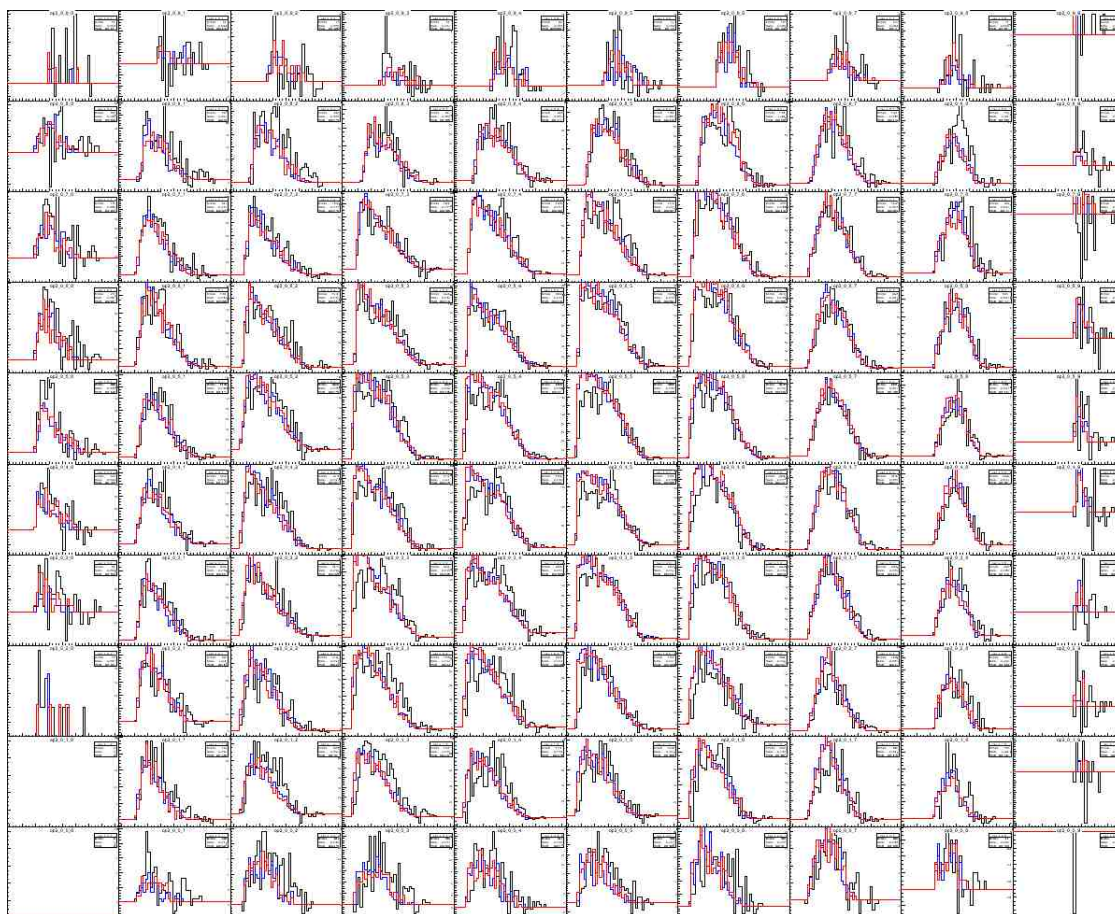


Figure 4.27: The spectra of BigBite momenta (black-data, blue-DMT, red-MAID) cut in grid of ϕ_{tg} and θ_{tg} from Figure 4.26 on top of the cut applied in Figure 4.24. Each plot is positioned where the cut in ϕ_{tg} and θ_{tg} is made (corresponding to the grid drawn in Figure 4.26).

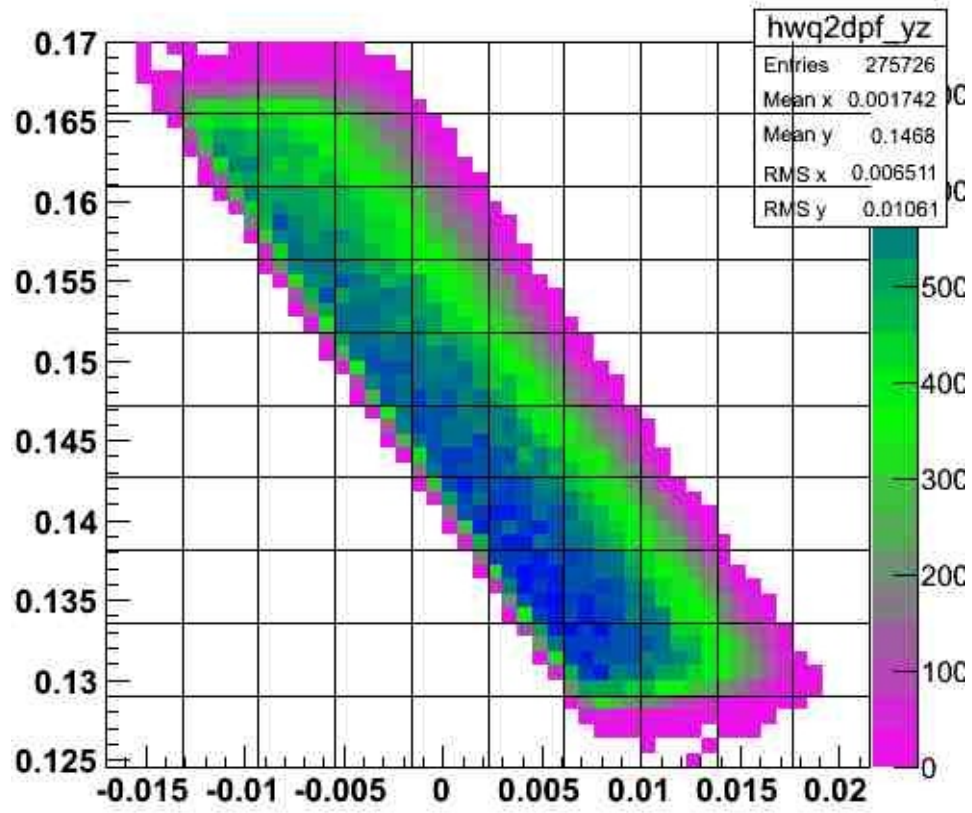


Figure 4.28: LHRs dp/p_0 (x-axis) versus Q^2 (y-axis). Cuts are the same as used in Figure 4.24.

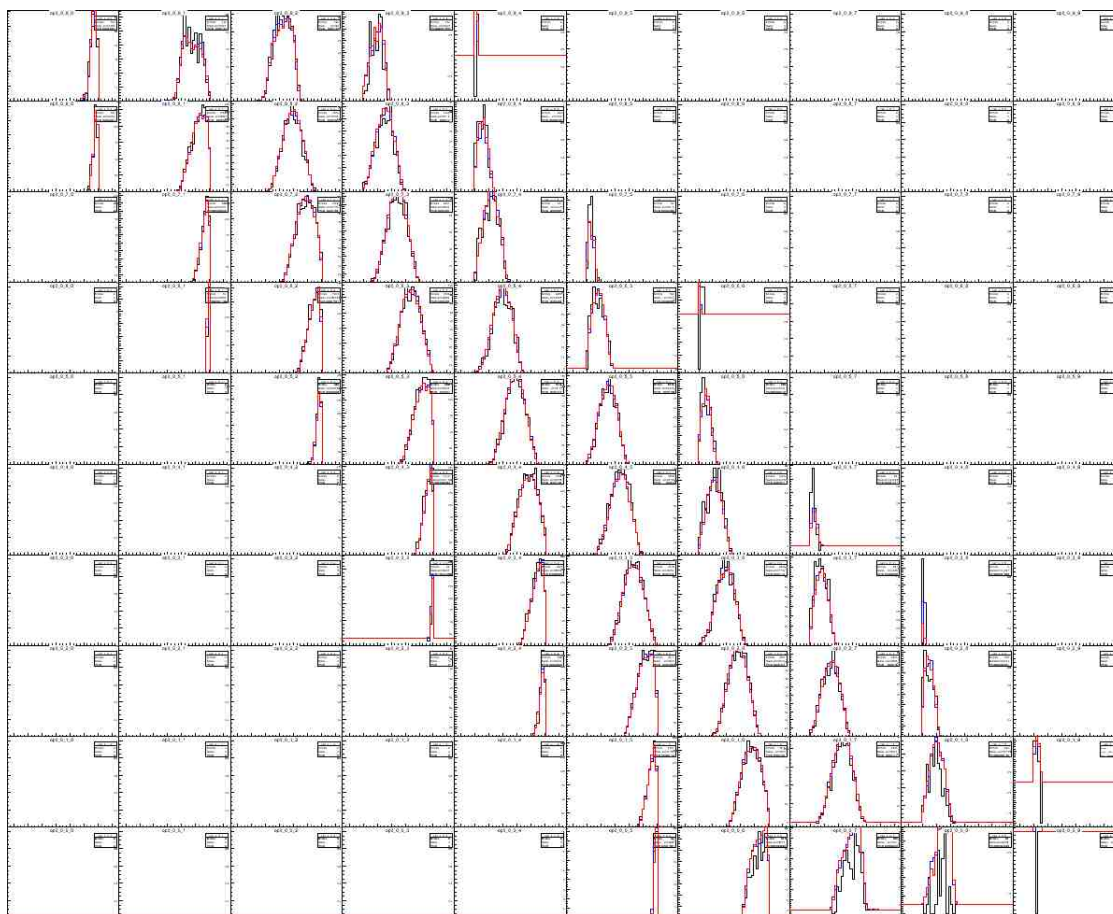


Figure 4.29: Comparison of simulated and measured W distributions (black-data, blue-DMT, red-MAID) for different cuts in the grid of dp/p_0 and Q^2 shown in Figure 4.28 in addition to the cut applied in Figure 4.24. Each plot is positioned where the cut in dp/p_0 and Q^2 is made (corresponding to the grid drawn in Figure 4.28).

Chapter 5

Cross Section and Radiative Correction

The five-fold differential cross section for pion-electroproduction using a polarized electron beam can be written as [40]

$$\frac{d\sigma}{d\Omega_e dE' d\Omega_\pi^*} = \Gamma \frac{d\sigma_v}{d\Omega_\pi^*} \quad (5.1)$$

where

$$\frac{d\sigma_v}{d\Omega_\pi^*} = \frac{d\sigma_T}{d\Omega_\pi^*} + \epsilon_L \frac{d\sigma_L}{d\Omega_\pi^*} + [2\epsilon_L(1 + \epsilon)]^{1/2} \frac{d\sigma_{LT}}{d\Omega_\pi^*} \cos\phi + \epsilon \frac{d\sigma_{TT}}{d\Omega_\pi^*} \cos 2\phi + h \sqrt{2\epsilon_L(1 - \epsilon)} \frac{d\sigma_{LT'}}{d\Omega_\pi^*} \sin\phi_\pi^* \quad (5.2)$$

The electron variables are defined in the laboratory system and the pion variables are defined in the pion-nucleon center of mass system designated by $*$, as shown schematically in figure 5.1, and h is beam helicity. The last term will be averaged out (helicity average is about zero) and not considered in this analysis. The two-fold differential cross sections (or structure functions) are defined in terms of the pion multipole amplitudes [40], which are functions of the two kinematic variables W , the invariant mass or cm energy of the pion-nucleon system,

and the four momentum Q^2 . These quantities are defined as

$$W^2 = -Q^2 + 2m\nu + m^2 \quad (5.3)$$

$$Q^2 = 4EE' \sin^2 \frac{\theta_e}{2} \quad (5.4)$$

where m is the proton mass, $\nu = E - E'$, $Q^2 = -q^2$, $q^2 = \nu^2 - |\vec{q}|^2$ and θ_e is the electron scattering angle, E is the electron beam energy, and E' is the scattered electron energy, which is defined as

$$E' = \frac{E - \frac{W^2 - m^2}{2m}}{1 + \frac{2E}{m} \sin^2 \frac{\theta_e}{2}} \quad (5.5)$$

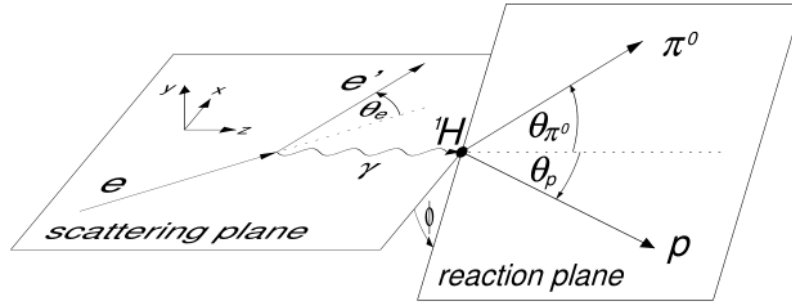


Figure 5.1: A schematic of the electron scattering and pion-nucleon reaction plane. Figure is from ref. [13]

The transverse and longitudinal photon polarization parameters, ϵ and ϵ_L , and the virtual flux factor, Γ are defined as

$$\epsilon = \frac{1}{1 + 2\bar{q}^2/Q^2 \tan^2 \frac{\theta_e}{2}} \quad (5.6)$$

$$\epsilon_L = \frac{Q^2}{\nu_{cm}^2} \epsilon \quad (5.7)$$

$$\Gamma = \frac{\alpha E' k_\gamma}{2\pi^2 E Q^2 (1 - \epsilon)} \quad (5.8)$$

with

$$k_\gamma = \frac{W^2 - m^2}{2m} \quad (5.9)$$

$$\nu_{cm} = \frac{W^2 - m^2 - Q^2}{2W} \quad (5.10)$$

The out of plane ϕ_π^* dependence of the cross section is used to separate the structure functions $\sigma_T + \epsilon_L \sigma_L$, σ_{TT} and σ_{LT} . The helicity dependent $\sigma_{LT'}$ structure function is discussed in ref. [21]. Threshold measurements are made as a function of Q^2 and W . The minimum energy, W_{th} , to produce a pion in the CM is $W_{th} = m + m_{\pi^0} = 1.07326$ GeV.

5.1 Background Subtraction

Background is of two types. One type is due to unwanted events that lie in the time of flight window due to accidental coincidences. These are reduced by taking counts from out of the time-of-flight window and subtracting them from the time-of-flight peak. There is also background due to real coincidences from quasi elastic pion production from the aluminum foil which serves as the entrance and exit window separating the cryogenic liquid hydrogen from vacuum. This background is comparable to the cross section near threshold. As shown in figure 5.2, after subtracting out the accidental events and putting a vertex cut on the middle 4cm of the 6cm liquid hydrogen target to remove real events from the window, events are still observed in the missing mass spectrum below the sharp missing mass pion peak. This may be due to the tail of quasi-elastic pion production from the

aluminum window. π^0 mass).

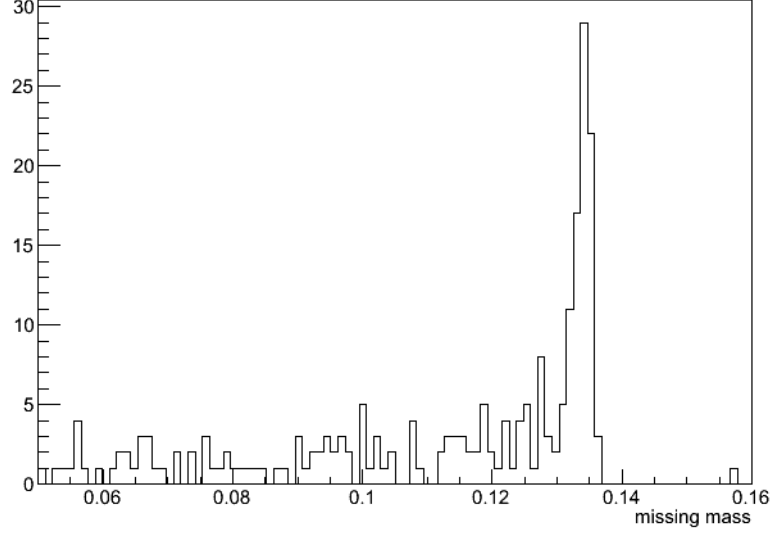


Figure 5.2: Missing mass[GeV/c^2] spectrum with $W_{th} < W < W_{th} + 2 MeV$ of middle 4cm (out of 6cm) liquid hydrogen target from one run.

The method used to subtract this background is now discussed. Dummy target data was taken on two pieces of aluminum foil separated by 6cm. However, insufficient statistics were taken to subtract background on a bin by bin basis. By summing over pion solid angle Ω_π^* and summing over Q and finely binned in W , there are enough statistics to determine an average distribution and subtract it from the missing mass spectrum. This method is justified by considering the distributions in figure 5.3 and 5.4

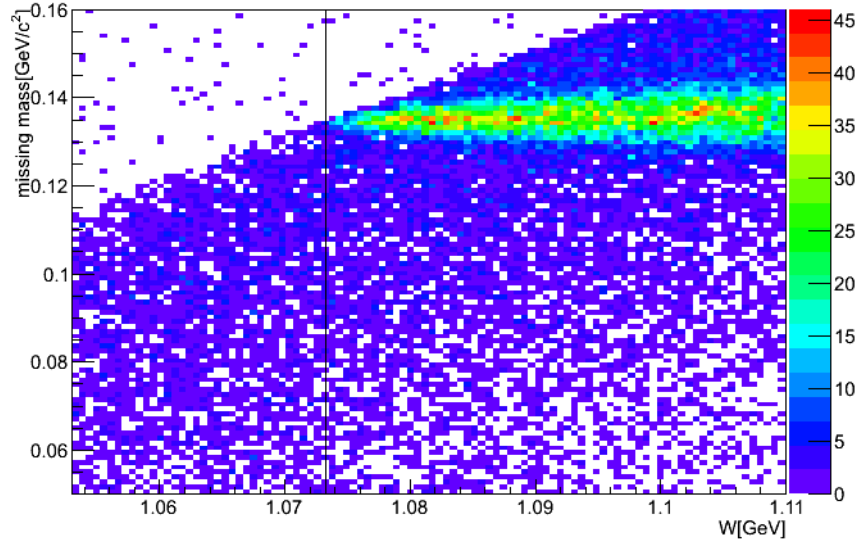


Figure 5.3: Scattered plot of missing mass versus W of liquid hydrogen target. The vertical line at 1.07326 shows the threshold.

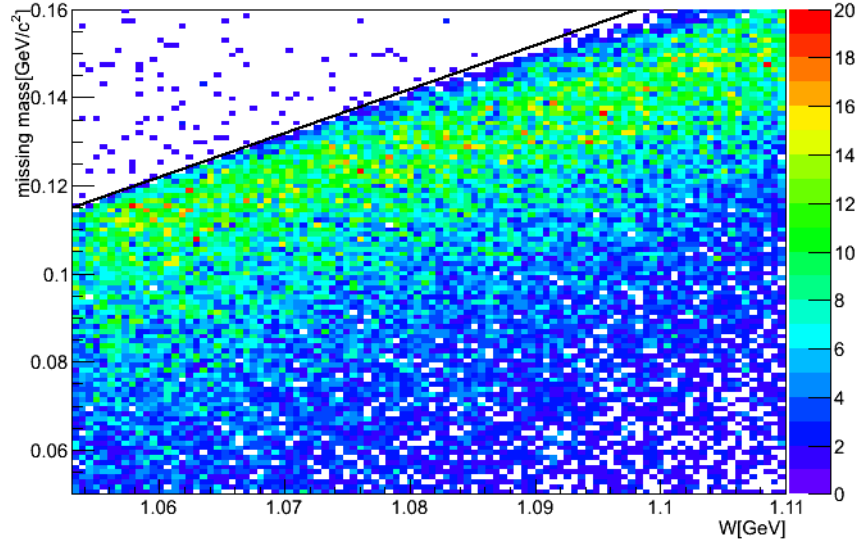


Figure 5.4: Scattered plot of missing mass versus W of dummy target (2 aluminum foils).

Also show in the figure, a black line slope=1 for reference.

From the figure 5.4, it can be shown that in the region from $W = W_{th} - 13 \text{ MeV}$ to $W = W_{th} + 20 \text{ MeV}$, the amount of the background is constant versus W , but the missing mass is slowly and linearly going up as W goes from 12 below threshold to 2 MeV below threshold. Before the data are averaged over 10 MeV , the missing mass is shifted according to the equation W

$$mm_{av0} = mm - (W - W_{th}). \quad (5.11)$$

Now the average is referenced to $W = W_{th}$. For each W bin, the average background is moved up

$$mm_{av} = mm_{av0} + (W - W_{th}) \quad (5.12)$$

before being used for background subtraction. This shift is clearly not as good at high W as can be seen in figure 5.4 because the band slowly deviates from the black line (slope=1) and the distribution also changes. The density of the band is slowly moving down from upper edge so another method would be needed. However, at high W , this background is much smaller compared to the true events and, therefore, we have ignored this correction. A comparison of this approximate method using a 4cm and 6cm target cut with the method using the dummy target for a 6 cm cut is shown in figure 5.1. The methods are quite similar within statistics.

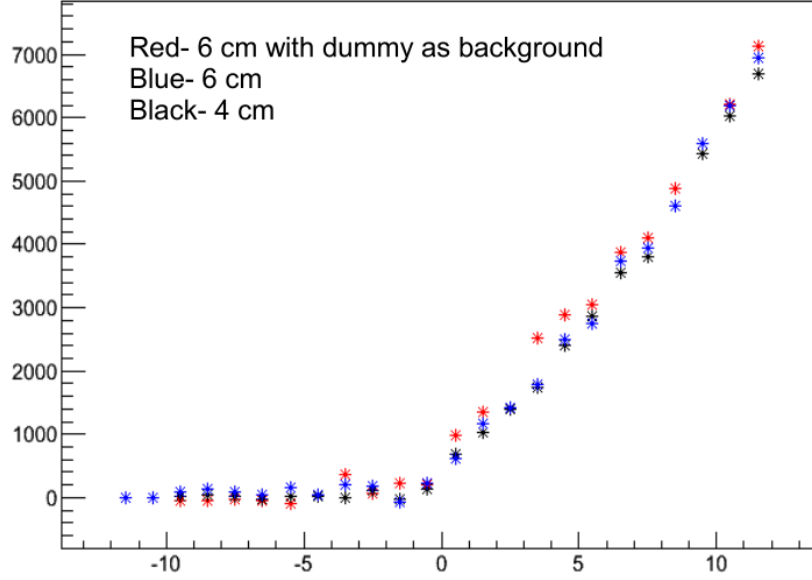


Figure 5.5: Count of missing mass in region ± 10 MeV around π^0 mass (y-axis) versus $W - W_{th}$ [MeV] (x-axis). For red star point, the background is taken from dummy target. For blue and black star, use the background subtraction method mention in section 5.1.

5.2 Radiative Corrections

The internal radiative correction, additional photon leg in Feynman diagram, was calculated using EXCLURAD [41, 42] and applied to the measured differential cross section bin by bin before perform the fitting. EXCLURAD is a code written in fortran for calculating the radiative corrections to exclusive electroproduction of pions on a nucleon. EXCLURAD uses a covariant infrared divergence cancellation procedure proposed by Bardin and Shumeiko in ref. [43]. This leads to an independence of the parameter that splits soft and hard regions of radiated photons. The physics models (ChPT, MAID, DMT in this case) were also used as input in EXCLURAD calculation. Figure 5.6 shows the different correc-

tion factors resulting from different physics models. The largest model dependence occurs at small and large ϕ^* where events are fewest and inconsequential. The external radiation corrections were made in the simulation calculation.

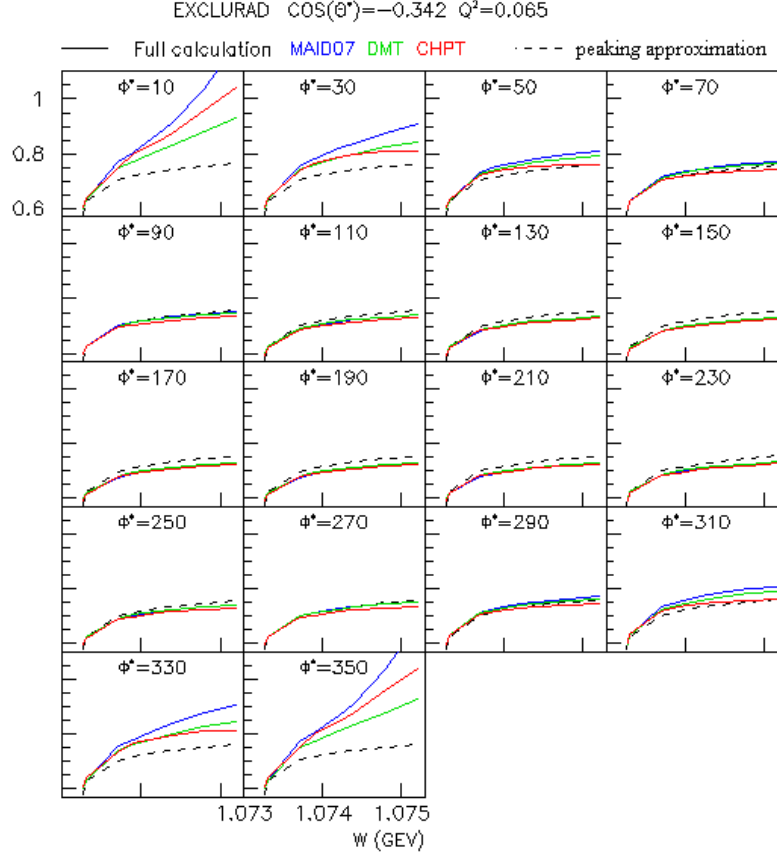


Figure 5.6: Example of EXCLURAD correction factors (y-axis) versus W (x-axis) for different ϕ^* . Figure is from [43].

5.3 Cross Section Measurement

It is accepted practice to bin the differential cross section in the kinematic variables ΔQ^2 , ΔW , and $\Delta \phi_e$ instead of $\Delta \cos \theta_e$, $\Delta \phi_e$ and $\Delta E'$. The transformation of variables $(\cos \theta_e, E') \rightarrow$

(Q^2, W) in (6.1) uses the Jacobian $J(Q^2, W)$

$$\frac{d\sigma}{d\Omega_e d\Omega_\pi^* dE'} = \frac{d\sigma}{dQ^2 dW d\phi_e d\Omega_\pi^*} \frac{1}{J(Q^2, W)} \quad (5.13)$$

where

$$J(Q^2, W) = \frac{W}{2mEE'} \quad (5.14)$$

W was divided into bins of 1 *MeV*; the first bin was centered at $W_{th} + 0.5$ *MeV* and the highest at 29.5 *MeV* above threshold. $\cos(\theta^*)$ was divided into 9 bins and ϕ^* into 18 bins. Q^2 and ϕ_e were binned a little differently due to the shape of acceptance.

Table 5.1: Q^2 and ϕ_e bins

left HRS angle(deg)	$Q^2(GeV/c)^2$	$\phi_e(rad)$
12.5	0.0475 to 0.0525	-0.28 to 0.28
	0.0525 to 0.0625	-0.28 to 0.28
	0.0625 to 0.0675	-0.28 to 0.28
14.5	0.0625 to 0.07	-0.25 to 0.25
	0.07 to 0.08	-0.25 to 0.25
	0.08 to 0.09	-0.25 to 0.25
16.5	0.0825 to 0.09	-0.22 to 0.22
	0.09 to 0.1	-0.22 to 0.22
	0.1 to 0.11	-0.22 to 0.2
20.5	0.13 to 0.14	-0.18 to 0.18
	0.14 to 0.15	-0.18 to 0.18
	0.15 to 0.16	-0.18 to 0.18

It is a good assumption that only s- and p-waves contribute to the structure functions $\sigma_T + \epsilon\sigma_L, \sigma_{TT}$ and σ_{LT} . Therefore, the cross section can be written as a sum over Legendre

polynomials up to $L=2$,

$$\begin{aligned} \frac{d\sigma}{d\Omega_\pi^*} = & \frac{p_\pi^*}{k_\gamma^*} (A_0^{T+L} + A_1^{T+L} P_1(\cos\theta^*)) + A_2^{T+L} P_2(\cos\theta^*) \\ & + \epsilon A_0^{TT} \sin^2\theta^* \cos 2\phi^* + \sqrt{2\epsilon_L(1+\epsilon)} (A_0^{LT} + A_1^{LT} P_1(\cos\theta^*)) \sin\theta^* \cos\phi^* \end{aligned} \quad (5.15)$$

where p_π^* is the π^0 momentum in the pion nucleon center of mass system

$$p_\pi^* = ((W^2 + m_\pi^2 - m^2)^2 / (2W)^2 - m_\pi^2)^{1/2} \quad (5.16)$$

and k_γ^* is the virtual photon momentum in pion nucleon center of mass system

$$k_\gamma^* = (m/W) |\vec{q}| \quad (5.17)$$

The measured cross section

$$\frac{d\sigma}{dQ^2 dW d\phi_e d\Omega_\pi^*} = \frac{N}{\Delta Q^2 \Delta W \Delta \phi_e \Delta \Omega_\pi^*} \frac{eA}{N_A \rho t C \epsilon (1-D) R} \frac{1}{f_{acc}} \quad (5.18)$$

is fitted to (5.15). Here e is the electron charge, A is the atomic weight of H, N_A is the Avogadro's number, ρt is the target thickness, C is the accumulated charge, ϵ is the overall efficiency (the factors in Table 4.1), D is the dead time, R is the radiative correction, f_{acc} is acceptance function defined in (4.6), and N is the yield summed over all runs with the same kinematics.

Chapter 6

Results and Conclusion

In this chapter, typical results are presented. Figure 6.1 shows the measured total differential cross sections at $Q^2 = 0.065 \text{ GeV}/c^2$ and $W = 1076.75 \text{ GeV}$ ($\Delta W = 3.5 \text{ MeV}$ above threshold) plotted as functions of $\cos(\theta^*)$ and ϕ^* .

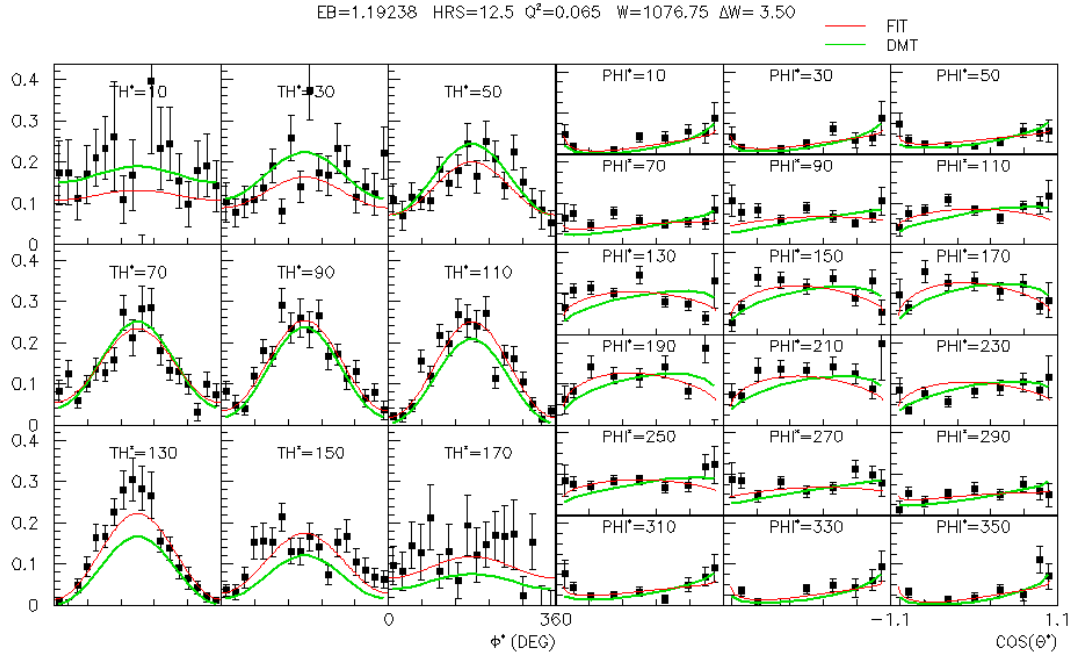


Figure 6.1: Comparison of measured angular distributions of the differential cross sections (black points) and DMT model (green line). Only statistical errors are shown. The red curves are determined from Legendre polynomial fits to the data.

The differential cross sections were fitted with the form in Eq.(5.15) in order to extract partial wave information about the structure functions σ_{T+L} , σ_{TT} and σ_{LT} . Results of the Legendre fits (red curves in Figure 6.1) are shown in the Figure 6.2 together with results from similar fits to model cross sections from ChPT[28, 29], MAID and DMT.

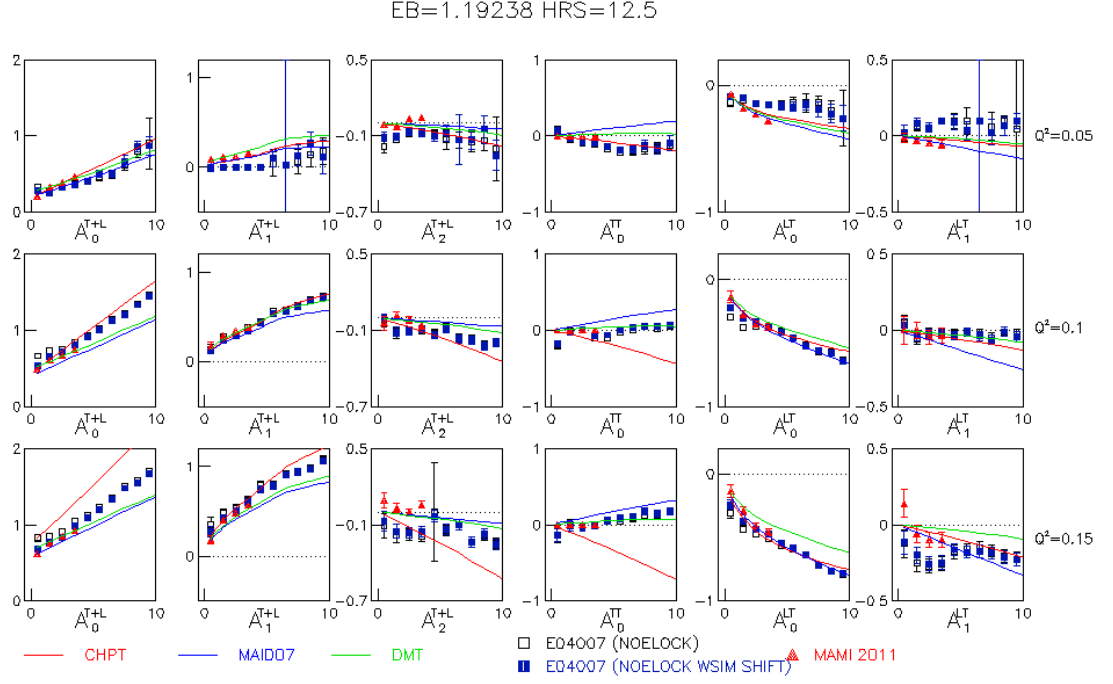


Figure 6.2: Results for the coefficients of the Legendre polynomial fits for Q^2 values corresponding to the MAMI 2011 values of $Q^2 = 0.05, 0.10, 0.15$ GeV/c² (1st, 2nd, 3rd row). Our data include runs for which the beam was not energy locked. The blue points show the effect of shifting the W calibration in the acceptance simulation by 220 keV in order to study systematics. Only statistical errors are shown. MAMI data are from ref. [44]. Only the data point is shown when the error is smaller than the size of the data point. Note that the coefficients are plotted on the y-axis and ΔW (MeV) is plotted on the x-axis. Each plot is labeled with the Legendre coefficient that is plotted.

We may obtain the total cross sections from the A_0^{T+L} Legendre coefficient:

$$\sigma_{total} = 4\pi \frac{p_\pi^*}{k_\gamma^*} A_0^{T+L} \quad (6.1)$$

These are shown in Figures 6.3, where several systematic effects are discussed. At the beginning of the experiment there was no energy lock on the electron beam, which resulted in drifts of up to 200 keV. For all runs the beam energy was available on an event-by-event basis and was used in the data analysis. However, for the acceptance simulation, only the overall spread in the beam energy was simulated, rather than the actual time dependence. This is one source of systematic error. Kinematic settings which did not have the energy lock were repeated later in the experiment, but with much lower statistics.

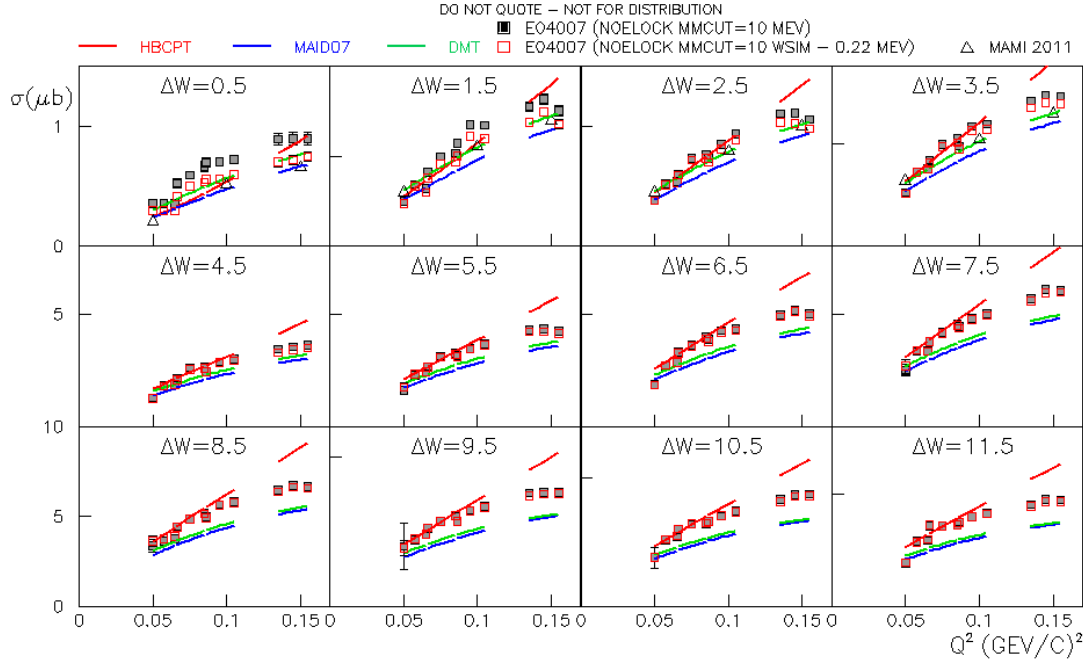


Figure 6.3: Total cross sections for first 12 W bins plotted versus Q^2 . The open squares show the effect of shifting the W calibration in the simulation by 220 keV. This illustrates the importance of consistency between the simulation and data in the LHRS momentum calibration.

Currently, the dominant source of systematic error in this experiment is the energy calibration. There are two kinds of calibration error: 1) Absolute calibration errors in the LHRS momentum reconstruction, and 2) relative shifts in the energy calibration between the simulation and data. Both effects can create large errors in extracted cross sections near a reaction threshold, since events (real or simulated) which are reconstructed below threshold are lost.

To check 1) we can replay elastic scattering data for various targets and check whether the target mass is correctly reconstructed. Our current analysis of elastic scattering on LH2

indicates the absolute W calibration may be high by ≈ 120 keV, while several solid target runs show smaller shifts (e.g. -22 keV for the tantalum (Ta) target in Figure 4.5). We still have to establish our uncertainty in absolute calibration by examining all LH2 and solid target runs.

It is easier to correct for the second source of energy calibration 2) mentioned above. We believe our GEANT3 simulation of the target environment and radiative and collisional energy losses is fairly robust, but we currently observe a 220 keV shift in the simulation of LH2 elastic scattering compared to data. The effect of this shift is shown in Figure 6.3 and needs to be investigated further. Clearly the effect is dominant at threshold and significant a few MeV above threshold but not noticeable at higher energies above threshold. To address this problem, a better calibration of the energy using more diagnostic tools is needed to determine how the energy may be varying from run to run.

6.1 Conclusion

The total cross section extracted from A_0^{T+L} shown in figure 6.3 from threshold to $\Delta W < 4.0$ MeV agrees with ChPT data from $Q^2 = 0.05$ to 0.10 $(GeV/c)^2$ and with the new MAMI[44] data up to $Q^2 = 0.15$ $(GeV/c)^2$ within experimental error. In the threshold region from $\Delta W = 4.0$ MeV to 10 MeV, the total cross section lies in between the faster rising ChPT prediction and the slower rising DMT and MAID07 model predictions.

The extracted Legendre polynomial coefficient A_0^{TT} shows a clear disagreement with ChPT for $\Delta W = 4.0$ MeV to 10 MeV and in increasing disagreement with higher Q^2 . The A_0^{TT} coefficient is in much closer agreement with DMT and not as close to MAID07 predictions over the same kinematic range. Except for the lowest $Q^2 = 0.05$ $(GeV/c)^2$, the second order Legendre polynomial coefficients A_1^{T+L} and A_0^{LT} lie very close to the ChPT

predictions from threshold up to $\Delta W = 10.0 MeV$.

In conclusion:

- 1) the present data are in agreement with the MAMI[44] total cross section measurements across the range of kinematics common to both measurements;
- 2) the present data agree with the total cross section predictions of ChPT (with LECs determined from earlier MAMI measurements [28,29]) for ΔW up to $4.0 MeV$ and $Q^2 \leq 0.1 [GeV/c]^2$; and
- 3) the present data disagree with the cross section predictions of MAID and DMT over almost the entire Q^2 and W range, with the disagreement becoming more pronounced with increasing Q^2 and W .

Since the quantitative predictions of ChPT depend upon the choice of LECs it remains to be seen whether fitting new LECs to the present data or including higher order terms in the calculations would improve the agreement between theory and experiment at higher W and Q^2 .

Bibliography

- [1] M. Fuchs *et al.*, Phys.Lett. B **368**, 20 (1996).
- [2] J. C. Bergstrom *et al.*, Phys. Rev. C **53**, R1052 (1996).
- [3] V. Bernard, N. Kaiser, and U.-G. Meißner, Phys. Lett. B **378**, 337 (1996).
- [4] M. O. Distler *et al.*, Phys. Rev. Lett. **80**, 2294 (1998).
- [5] H. B. van der Brink *et al.*, Phys. Rev. Lett. **74**, 3561 (1995).
- [6] H. Merkel, Pion threshold electro- and photo- production, Talk for the Chiral Dynamics 2000 Workshop.
- [7] H. Merkel *et al.*, Phys. Rev. Lett. **88**, 12301 (2002).
- [8] M. Fuchs *et al.*, Phys. Lett. B **368**, 20 (1996).
- [9] A. Vainsthein and V. Zakharov, Nucl. Phys. B **36**, 589 (1970).
- [10] P. de Baenst, Nucl. Phys. B **24**, 633 (1970).
- [11] R. Lindgren, Proposed Measurements of Electroproduction of π^0 near Threshold using a Large Acceptance Spectrometer, Talk for Chiral Dynamics 2006 Workshop,.
- [12] T. P. Welch *et al.*, Phys. Rev. Lett. **69**, 2761 (1992).
- [13] D. Crabb *et al.*, Precision Measurements of Electroproduction of π^0 near Threshold: A Test of Chiral QCD Dynamics, Proposal to Jefferson Lab PAC 25.
- [14] H. Fritzsch and M. Gell-Mann, Current algebra: Quarks and what else?,in Proc. XVI Int. Conf. om High Energy Physics, ed. J.D. Jackson and A. Roberts(National Accelerator Laboratory, Batavia, Ill.), 1972.
- [15] W. Marciano and H. Pagels, Phys. Rep. **36C**, 137 (1978).
- [16] A. S. Kronfeld and C. Quigg, Am. J. Phys. **78**, 1081 (2010).
- [17] wiki/Quark, <http://en.wikipedia.org/wiki/Quark>, [modified 14-July-2012].
- [18] J. Goldstone, A. Salam, and S. Weinberg, Phys. Rev. **127**, 965 (1962).
- [19] wiki/Effective field theory, http://en.wikipedia.org/wiki/Effective_field_theory, [modified 29-April-2012].

- [20] S. Scherer and M. R. Schindler, *A Primer for Chiral Perturbation Theory* (Springer-Verlag, Berlin Heidelberg, 2012).
- [21] M. H. Shabestari, Ph.D. thesis, University of Virginia, Charlottesville, Virginia, 2010.
- [22] J. Gasser and H. Leutwyler, *Annals of Physics* **158**, 142 (1984).
- [23] J. Gasser, M. E. Sainio, and A. Svarc, *Nucl. Phys. B* **307**, 779 (1988).
- [24] H. Georgi, *Phys. Lett. B* **240**, 447 (1990).
- [25] E. Jenkins and A. V. Manohar, *Nucl. Phys. B* **255**, 558 (1991).
- [26] V. Bernard, N. Kaiser, J. Kambor, and U.-G. Meißner, *Nucl. Phys. B* **388**, 315 (1992).
- [27] J. Gasser and H. Leutwyler, *Nucl. Phys. B* **250**, 465 (1985).
- [28] V. Bernard, N. Kaiser, and U.-G. Meißner, *Nucl. Phys. A* **607**, 379 (1996).
- [29] V. Bernard, N. Kaiser, and U.-G. Meißner, *Nucl. Phys. A* **633**, 695 (1998).
- [30] D. Drechsel, S. S. Kamalov, , and L. Tiator, *Eur. Phys. J. A* **34**, 69 (2007).
- [31] S. S. Kamalov *et al.*, *Phys. Lett. B* **522**, 27 (2001).
- [32] J. Alcorn *et al.*, *Nuclear Instruments and Methods in Physics Research A* **522**, 294 (2004).
- [33] D. J. J. de Lange *et al.*, *Nuclear Instruments and Methods in Physics Research A* **412**, 254 (1998).
- [34] D. Meekins, Hall A Target Configuration Report, JLAB, March 2008.
- [35] X. Qian, Ph.D. thesis, Duke University, Durham, NC, 2010.
- [36] R. Lindgren, Status of E04-007 : Threshold $H(e, e'p)\pi^0$, Talk for Hall A Collaboration Meeting, JLAB, June 2008,.
- [37] N. Liyanage, *Optics calibration of the Hall A High Resolution Spectrometers Using the New Optimizer*, 2002.
- [38] Dell'Orso *et al.*, *Nuclear Instruments and Methods in Physics Research A* **287**, 431 (1990).
- [39] W. R. Leo, *Techniques for Nuclear and Particle Physics Experiment* (Springer, Berlin Heidelberg, 1987).
- [40] D. Drechsel and L. Tiator, *J. Phys. G: Nucl. Part. Phys.* **18**, 449 (1992).
- [41] A. Afanasev, I. Akushevich, V. Burkert, and K. Joo, *Phys. Rev. D* **66**, 074004 (2002).
- [42] <http://www.jlab.org/RC/exclurad/>.
- [43] http://clasweb.jlab.org/wiki/index.php/Radiative_Corrections.
- [44] H. Merkel *et al.*, arXiv:1109.5075v1 [nucl-ex].